Neutron Reactions in Superheated Fluids

By:

Clayton Blaine Coutu

A thesis submitted in partial fulfillment of the requirements for the degree of

Master of Science

Department of Physics
University of Alberta

Abstract

The PICO-60 experiment offers world leading sensitivity to the spin-dependent Weakly Interacting Massive Particle (WIMP) search, looking for the direct measurement of dark matter nuclear recoils with protons. The primary background in moderately super-heated C_3F_8 bubble chambers are neutrons, which can produce a signal indistinguishable from a dark matter candidate. To study the detectors response to neutrons, I show the relationship between bubble multiplicity and neutron energy is non-linear; meaning there is insufficient information in multi-bubble events to reconstruct the primary energy. This observation is explained by nuclear reactions at energies above 1.5 MeV, from fast neutrons depositing more energy above threshold into a single bubble event. Studying the acoustic energy emitted from nuclear reactions, I predict that these fast neutrons can be identified in the tail of the acoustic parameter (AP) distribution, which PICO originally uses to identify background alphas associated with the decay of ^{222}Rn. In an attempt to reconstruct the neutrons origin, a technique to assign 3D coordinates to multi-bubble events is described using PICO-60 data and compared with Monte-Carlo simulations. The result is inconclusive, primarily because of a lack of statistics in the neutron calibration data. Finally, the commissioning of the PICO-40L detector at SNOLAB is discussed, focusing on my contributions to the thermal and camera installation. The new detector offers increased sensitivity to the dark matter search, and will continue the neutron AP and multi-bubble analysis presented.

Preface

The research presented is part of an international collaboration called PICO, with Professor C. Krauss. The contributions of my work are:

- I extended the GEANT4 simulations developed by PICO, Chapter 7, to provide information relating to neutron reactions. Including the type of reaction taking place and the energy of the neutron as it enters the detector volume. I prepared/ran all of the simulation and the analysis presented is my work.

- I extended the molecular dynamics model developed by PICO, Chapter 8, to describe nuclear reactions from fast neutrons. I fit the simulation to the PICO-60 data and the associated analysis is my original work.

- I extended the 3D reconstruction tool developed by P. Mitra to assign coordinates to multi-bubble events, Chapter 9. Using these 3D coordinates, I developed the minimization algorithms using python packages and presented my own analysis.

- My contribution to the commissioning of PICO-40L is presented in Chapter 10. I worked on preparing/shipping the HDPE and copper components at the University of Alberta. I worked onsite at SNOLAB for four months to install the Cold flange housing, the instrumentation flange, the feed-through flange, and additional thermal components. I also contributed to the installation of the camera systems, and worked with other collaborators to monitor the detector during engineering runs.

The PICO-60 and 40L 3D renderings presented in Figures 5 and 42 are provided by PICO collaborators, aside from my own labels added to Figure 42. The PICO-60 geometry used in GEANT4 is maintained by PICO collaborators. The original molecular dynamics model was developed by PICO collaborators. The 3D bubble reconstruction tool is built

upon the original work done by P. Mitra. The design of the PICO-60 and PICO-40L detectors belongs to the PICO collaboration.

I certify that the work presented is my own and to my knowledge has not been submitted to any other university or publisher. All 3^{rd} party information has been acknowledged.

Dedication

My education has been made possible thanks to the support from countless individuals over the years. Including, but not limited to: high school teachers, university professors, technicians, friends, grandparents, and extended family. A list too long for names to be provided here, but it cannot be missed that I appreciate all the help I've received.

My direct family I will put on the spot for so many reasons, however I'll keep it short. To my father Blaine Coutu, who passed many years ago to cancer; to my dad Russell Aulstead, who raised and cared for me as his son; to my mom Tracey Aulstead, whose unwavering support of her children has allowed us to experience fulfilling and happy lives; to my sister Becky, who is a great role model and is always there for me; to my wife Alizeh, who supports my decisions and is quick to help; and to my in-laws, who accepted me into their family.

"Doing science as if people matter."

- Dr. Margaret-Ann Armour (1939-2019)

Acknowledgement

I hereby recognize that the University of Alberta, to which my education was made possible, is founded upon the lands of First Nations. I'm thankful to those who've nurtured and cared for this land long before my time, and respect the history of those recognized or remain unrecognized.

I would like to thank my sponsors who made the Queen Elizabeth II Graduate, the Alberta Graduate Excellence, and the Baker Hughes Indigenous scholarships possible. The support provided allowed me to focus on my research and insured financial stability for my wife and I during the Covid-19 pandemic.

I'd like to give a special thanks to Carsten Krauss and Scott Fallows, who are quick to provide assistance, feedback, and thoughtful discussion. Additional thanks goes to the PICO collaboration, for the opportunity to work on an exciting research topic, and SNOLAB personal who make clean research in an active mine possible.

Finally, I'd like to thank the University of Alberta's Department of Physics and my research committee. The department has offered me extensive resources during my BSc and MSc education that I'm incredible grateful for.

Contents

List of Figures

List of Tables

1 Introduction

The incomplete mass budget of the universe motivates the scientific community to search for particles beyond the Standard Model of particle physics (SM). Dark matter (DM) fits in as an undetected mass not described by SM, but is known to exist because of its gravitational presence. The task for experimental research, is to design a detector that offers an interaction probability consistent with the phase space of dark matter candidates. This challenge forces experiments deep underground to shield from the radioactivity of the Earth's surface, while also requiring a large target mass to increase the likely hood of detection.

The work presented in this thesis addresses how moderately super-heated bubble chambers (BC) detect neutrons. The motivation is that neutrons persist as the dominant background in BC and can mimic the DM signal. The neutron analysis will explain why bubble multiplicity and cluster size cannot be directly correlated to primary neutron energy; how the presence of neutron induced nuclear reactions, offers an explanation for events in the acoustic parameter distribution (AP) measured by PICO; and that the direction of neutron sources cannot be reconstructed by minimizing a line about the center of gravity for a cluster of bubbles.

The topic of DM is first introduced in Chapter 2, using evidence from astronomy to present the cosmological problem of missing matter. The difficulty in DM direct detection is described using cross sections from leading experiments. This leads into Chapter 3, providing a discussion of experimental techniques used in DM searches. Here the PICO-60 detector is described, by introducing the technology and how a WIMP candidate would be identified. This extends into Chapter 4, where backgrounds in BC are explained to motivate analysis of neutron reactions.

Chapter 5 describes the operation of PICO-60 and how the analysis will improve the understanding of the detectors response to neutrons. In Chapter 6, a GEANT4 simulation

of neutrons in a tank of C_3F_8 demonstrates that bubble multiplicity and cluster size alone do not provide sufficient information to reconstruct primary neutron energy. Nuclear reactions from fast neutrons are then introduced and to interpret how these processes are observed in PICO-60, Chapter 7 presents simulations using the PICO-60 geometry. This provides a data set to explain how neutrons undergoing nuclear reactions can be identified in the log(AP) distribution.

The acoustic parameter (AP), first introduced in Chapter 3, is described in detail in Chapter 8. This section outlines how to model AP using molecular dynamic simulations, and what simplifications are used to extend the analysis to neutron reactions. The outcome is a model that shows consistency with PICO-60 data, concluding that neutrons could explain tail events outside the nuclear recoil and background alpha spectra.

To finish the neutron study, Chapter 9 describes a technique to 3D reconstruct multi-bubble events from PICO-60 data. The center of gravity for these 3D coordinates is used to generate a line through the bubble cluster. The direction of this line is adjusted to minimize the distance of each bubble, and then compared to the known source placement by calculating the opening angle. The analysis is first run on simulated data using both a large C_3F_8 body and the PICO-60 geometry. Comparing the simulation's opening angle to the real data is found to be inconclusive, primarily due to a limited data set.

The end to this thesis presents the construction and commissioning of PICO-40L at SNOLAB. The focus is on the thermal and camera integration, introducing how each system works and key steps involved in the assembly. Also included is the first look at an event captured during an engineering run, and describes how the calibration runs will be used to further the neutron log(AP) and direction analysis presented in this work.

2 Astronomical Problem: Missing Matter

Measurements in astrophysics indicate an abundance of matter in the universe that does not interact directly through electromagnetic forces. This claim stems from analyzing moving objects [1], mass predictions from gravitation lensing [2], and the cosmic microwave background [3]. The mounting data suggest a new form of matter not described by the SM that does not absorb or emit light, awarding it the title of "Dark Matter".

2.1 Rotating Objects

By the 1900s, progressing technology made it possible to separate light into a sequence of emission/absorption lines, called spectroscopy. Applying spectroscopy to light collected from galaxies M31 (Andromeda) and NGC 4594 (Sombrero), V. Slipher [4] and M. Wolf [5] in 1914 provided evidence that stars and gases in galaxies are rotating about their center position; confirmed 4 years later by F. Pease [6]. Slipher's research also indicated that some nebula showed a shift in the measured spectra, which wasn't tied to distance until E. Hubble and L. Milton's 1931 publication "The Velocity-Distance Relation among Extra-Galactic Nebulea"[7]; introducing the concept of Red-Shift to refer to spectra shifted towards the infrared, associated with objects moving away from an observer.

Spectroscopy led to one of the first instances where dark matter appears in literature, accredited to F. Zwicky in his 1933 publication "Die Rotverschiebung von extragalaktischen Nebeln"[1] [1]. He demonstrates, using the Virial Theorem to calculate the velocity of objects in the Coma Cluster, that the average density of matter in the Coma System is at least 400 times greater than predictions from measuring the amount of luminous matter. The interpretation was very surprising, because it suggests that DM exists with a greater density than luminous matter. The hypothesized dark matter gained support almost 30 years

[1] The Redshift of Extragalactic Nebulae.

later after detailed measurements of galactic rotations curves was published in 1963 by V. Rubin, et al. [8]; who studied dwarf spiral galaxy NGC 6503, see Figure 1.

Figure 1: Dwarf spiral galaxy NGC 6503. Credit: Hubble Space Telescope (NASA, ESA). Measuring the orbital velocity of objects around the galaxies core, it was discovered that matter farther away does not rotate slower. To explain this observation, the dominant matter distribution in the galaxy must not emit or absorb light and must extend to larger distances.

NGC 6503 was used to research the velocity of objects rotating about a galaxies center of (visible) mass. With the framework of Newtonian mechanics and the application of Kepler's laws, the outcome should have been quite clear: as objects get farther away from the galactic core they should move slower thanks to the well understood $\frac{1}{\sqrt{r}}$ relationship. However this was not observed, because at larger distances the velocities increase and level off. To interpret this observation there needs to be a large distribution of undetected mass, agreeing with Zwicky's prediction.

The analysis of rotation curves has since been conducted with other galaxies [9], showing consistent results that favour the presence of dark matter.

2.2 Gravitational Lensing

The deflection of light, propagating through an in-homogeneous gravitational field, was one of the first successful predictions of General Relativity (GR) since it's publication by A. Einstein in 1915. Interestingly, the bending of light around a gravitating mass was acknowledged in 1804 by German astronomer J. Soldner, who used classical mechanics to calculate the deviation in angular position of stars [10]. Soldner's derivation predicted that a light ray passing by the sun should deflect by approximately 0.85 arc seconds.

Einstein independently arrived at the same conclusion, however when cross referencing with GR he predicted an extra factor of 2; Therefore, according to GR the deflection should be approximately 1.7 arc seconds. This was experimentally confirmed in 1919, by measuring light from a distant star passing by the sun during a solar eclipse [11].

This bending of light is refereed to as gravitational lensing. The phenomenon implies that light from a distant object can follow multiple paths before reaching an observer. For example, in Figure 2 light from the distant galaxy (blue) is bending around the foreground object (red). The resulting image is a ring, because the light can travel around the obstruction to the left (top) or right (bottom) equally. The observation is an image of a distant object appearing duplicated, which becomes more pronounced when the light passes by massive or compact objects.

At the time (1920's) little was known about galaxies, so the multiple images predicted by GR didn't receive much attention. Light from a distant star could pass around a foreground star producing a duplicated image, but the angular separation between these two images would be difficult for telescopes to resolve [2].

Requiring sufficiently massive foreground objects to observe lensing, returns the discussion to F. Zwicky. In 1937 he predicted that the deflection of light around galaxies (called nebula at the time of writing) offer a better chance to observe gravitational lens-

ing [12, 13]. Zwicky's insight stems from his earlier work where he determined the mass content of the Coma Cluster to be larger than previous estimates. These publications introduced the first attempt to use gravitational lensing to directly determine the mass of extra-galactic nebulea (galaxies.)

Figure 2: Luminous red galaxy (LRG) 3-757. Credit: Hubble Space Telescope (NASA, ESA). Gravitational lensing of background object (blue galaxy) due to foreground structure (LRG 3-757). Light from the distant galaxy has to pass by LRG 3-757 on its trajectory to Earth. The strong gravitational field bends the light paths around the object, resulting in duplicated and/or smeared images.

Zwicky's prediction did not catch on for some time, because it wasn't until 1979 when Walsh et al., [14] observed the first multiple-image system. This discovery opened up the field of gravitational lensing, because it became evident that the deflection angle of light is dependent solely on the gravitational field of the impeding object, meaning the total matter density can be resolved.

Gravitational lensing now provides an effective probe to investigate the topic of DM. This technique compliments the rotation curve results, because lensing can estimate the total mass distribution of galaxy clusters [15, 16], supporting the existence of DM.

2.3 Cosmic Microwave Background

The denouement in DM evidence originates from the accidental discovery of the Cosmic Microwave Background (CMB). First predicted in 1948 by R. Alpherin et al. [17], the CMB was detected in 1964 by R. Wilson and A. Penzias [18] who measured excess noise in their 6 m horn antenna. After extensive attempts to reduce this background, they conceded that the signal was cosmic in origin. This was immediately picked up by R. Dicke et al. [19], who interpreted the signal as the CMB.

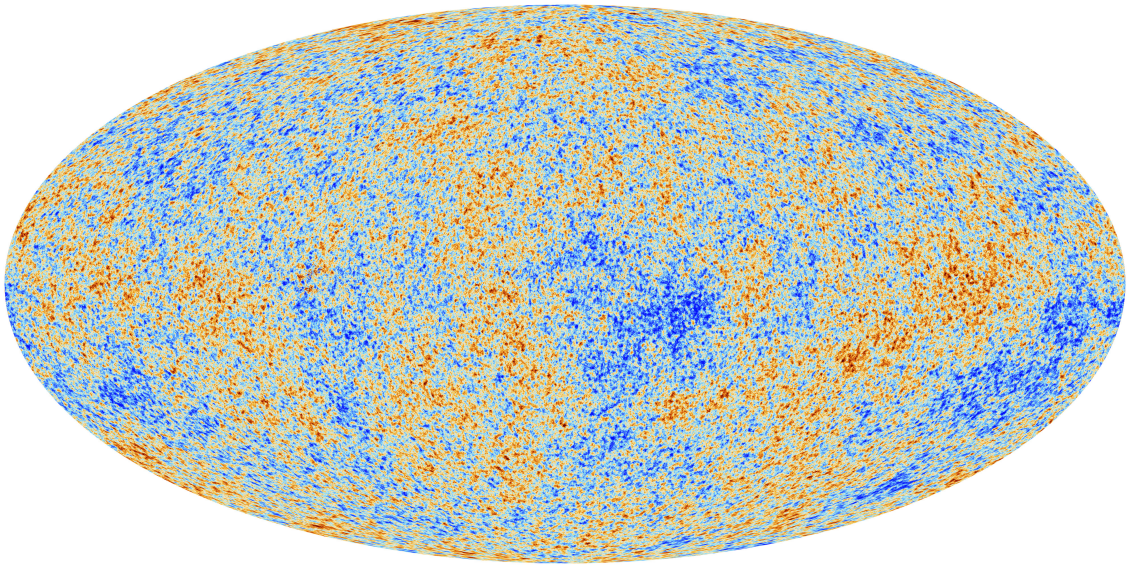

Figure 3: Cosmic Microwave Background. Credit: ESA and Planck Collaboration 2018. This image reveals the temperature fluctuations of the early universe.

The CMB reveals temperature fluctuations in the radiation left over from the big bang, which follows the spectrum of black body radiation at 2.73 K. During the early phases of the Universe (predating atoms, stars, and galaxies) photons could not propagate freely in the hot dense state of matter. With sufficient expansion of space, the Universe cooled enough for protons and electrons to merge. At this point, the newly formed atoms could no longer absorb thermal radiation, resulting in the free propagation of photons. These photons

remain, are propagating in all directions, and can be measured at microwave frequencies.

Initial attempts to understand the CMB in the 1970's failed, because the models relied upon purely baryonic matter which couldn't explain the small anisotropies being detected (upper limit estimates at the time). By the 1980's, the mounting evidence of DM reshaped these models to describe a universe dominated by cold dark matter (CDM) and not baryons.

CMB measurements have improved dramatically since then. The best results to date are from Plank (see Figure 3) and balloon experiments in Antarctica [3]. To study the matter content of the early Universe, the CMB is represented as a power spectrum; Where the energy density of baryonic and dark matter can be fit to best narrow down a model that describes cosmology. The fits presented by [3] are in excellent agreement with a dark matter filled Universe.

Based on the study of CMB we can conclude that the mass content of the Universe is greater than visible matter alone can account for, consistent with the conclusions from studying galaxy rotation curves and gravitational lensing.

2.4 Dark Matter

The mass budget of the universe has captivated the scientific community, because dark matter indicates the standard model of particle physics is incomplete; which does not contain a particle consistent with the properties that explain astronomical observations. However, when describing such an ambiguous topic its worth noting that dark matter could be a blanket term. What remains unclear is whether or not dark matter consists of one explicit form of matter or an assortment. There could be a large array of new physics beyond the standard model, which contain particles that simply do not interact electromagnetically. When a dark matter candidate is observed, its abundance might fall short of explaining the full cosmological picture.

This ambiguity has the scientific community pursuing a broad range of experiments, each aiming to provide insight to the nature of dark matter. A DM model consistent with the evidence previously highlighted, describes Cold Dark Matter (CDM) particles [20]. Cold is used here to describe DM that moves slow relative to the speed of light, allowing the particles to freeze out of thermal equilibrium following the big bang; sufficient cooling and expansion of the early universe meant DM production was no longer energetically favourable, "freezing" the total dark matter content.

A candidate for CDM is the Weakly Interacting Massive Particle; commonly abbreviated as WIMP [21, 22]. WIMPs are an extension to the standard model motivated by supersymmetry. The WIMP describes a form of matter that is collision-less (interacts via the weak force), electrically neutral (does not cool by emitting photons), non-baryonic (not composed of protons and neutrons) and is expected in a large mass range (GeV to TeV).

Several experiments are being conducted to search the parameter space of the WIMP, as discussed in the next section. The shared goal is for the direct observation of coherent elastic scattering of dark matter particles with normal standard model particles (like protons) via nuclear recoils. The engineering difficulty these experiments face is a result of the weak force, because the cross section for weak elastic scattering with ordinary matter falls in the range of 10^{-40}cm^2 to 10^{-50}cm^2 [20].

An example of the spin dependent WIMP-proton parameter space currently ruled out by leading experiments is shown in Figure 4. These exclusion curves are displayed in terms of cross section, which describes the interaction probability of dark matter with nucleons in the detector target (protons). This quantity, measured in units of barns (10^{-28} cm^2) and denoted σ, describes the probability that the collision of two particles will take place. This representation of data allows different experiments to readily compare results. The area above the curves is excluded by the respective experiments, providing an upper cross section limit in the dark matter search.

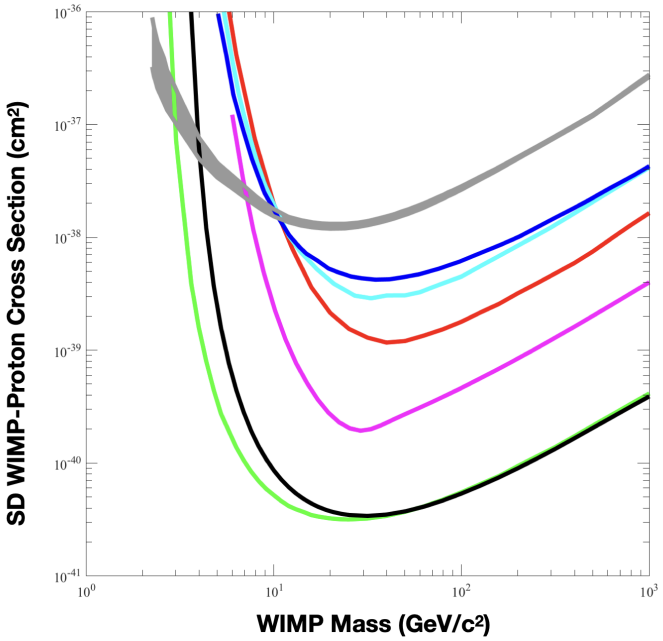

Figure 4: Exclusion curves for leading experiments spin dependent WIMP-proton cross sections. Black: PICO-60 2017 [23]. Green: PICO-60 2019 [24]. Blue: SIMPLE 2014 [25]. Grey: PICASSO 2017 [26]. Cyan: LUX 2016 [27]. Red: PandaX-II 2017 [28]. Magenta: XENON1T 2019 [29].

For example, if the WIMP had a mass on the order of 8 GeV/c^2, from Figure 4 the cross section must be less than 10^{-40} cm^2 or 1 femtobarn. Measuring such tiny interaction probabilities requires large experiments with very low intrinsic backgrounds, and have forced detectors deep underground to suppress external backgrounds that have cross sections as big as a barn.

3 The Search for Dark Matter

Advancements in technology continue to push the limits of particle detection by orders of magnitude in cross section, to directly observe a DM particle interaction. Collaborations around the world have put forward experiments for the dark matter search, each offering unique advantages that push the physics community towards the common goal.

3.1 Cryogenic Solid State Detectors

Experiments making use of semiconductors for the detection of particles are historically referred to as solid state detectors. The most common materials used are silicon and germanium. As ionizing radiation passes through the high density crystal target, electron-hole pairs are formed and can be collected by applying an electric field.

The advantage of using semiconductors is the energy required to create a free charge in the crystal is low when compared to gas targets. Silicon is popular because of it's availability, but Germanium is ideal because it offers a much higher atomic number; meaning the photoelectric cross section is greater than that of silicon. The main disadvantage to germanium is the cost.

To operate, a bias voltage is placed across the crystal to deplete the electron like pairs throughout the detector volume and to collect electrons from particle interactions. The technology offers a great advantage to the dark matter search due to the ability to detect very weak signals. The main background comes from β and gamma interactions, which can be identified as demonstrated by the CDMS experiment.

The superCDMS detector [30] makes use of germanium crystals operated at cryogenic temperatures to detect low mass particles, but they also incorporate superconducting transition edge sensors for the measurement of phonons. The phonons, together with the amplified electrical signal, can reject background events from β and gamma radiation to identify DM candidates.

3.2 Liquid/Noble Gas Detectors

Liquid phase detectors typically use noble elements like argon or xenon. The technology relies on capturing scintillating light generated from the excitation of the liquid atoms. To measure the amount of light generated in an event, photo multiplier tubes (PMT) or

silicon photo multipliers (SiPMs) are situated around the detector.

For example, DEAP3600 [31] uses liquid argon and is situated at SNOLAB in Sudbury Ontario. The experiment shifts the wavelength of the emited light to allow detection by the PMTs. Argon has the advantage of a large timing difference in the emission of scintillation light, which allows the use of pulse shape analysis techniques to cut backgrounds, not produced by nuclear recoils, from the data sample.

The use of xenon is competitive due to its level of purity and suppression of gamma interactions. For example, the XENON1T experiment [29] employed a time projection chamber (TPC) using xenon as a target, and was operated at INFN Laboratori Nazionali del Gran Sasso in Italy. The TPC used a liquid and a gas phase. When radiation interacts with the liquid, ionizing charges generate electrons and scintillation light; which is collected and designated S1. The electrons then drift upwards towards the gas phase, where they generate a second signal S2. Backgrounds are removed by first taking the ratio of S1/S2 to identify an event as either being a nuclear or electron recoil. Secondly, comparing the time delay between S1 to S2 the local region of the event can be identified, eliminating backgrounds originating from the detector itself.

3.3 Gas Detectors

Gas based detectors have a rich history in radiation detection, operating under the basic premise of collecting electrons and ions produced from the passage of particles. The technology has since been adapted by the NEWS-G collaboration [32], using a spherical proportional counter (SPC) for the detection of low mass dark matter.

The simplicity of the SPC offers a huge advantage in engineering because the scale of the detector can be increased without loss of sensitivity. In addition, due to the gas amplification the detector is sensitive to single electron events.

3.4 Moderately Superheated Fluids

The PICO-60 experiment was also located at SNOLAB. The collaboration has developed a moderately superheated liquid detector that is able to measure low energy nuclear recoils while being intrinsically insensitive to beta and gamma backgrounds [24].

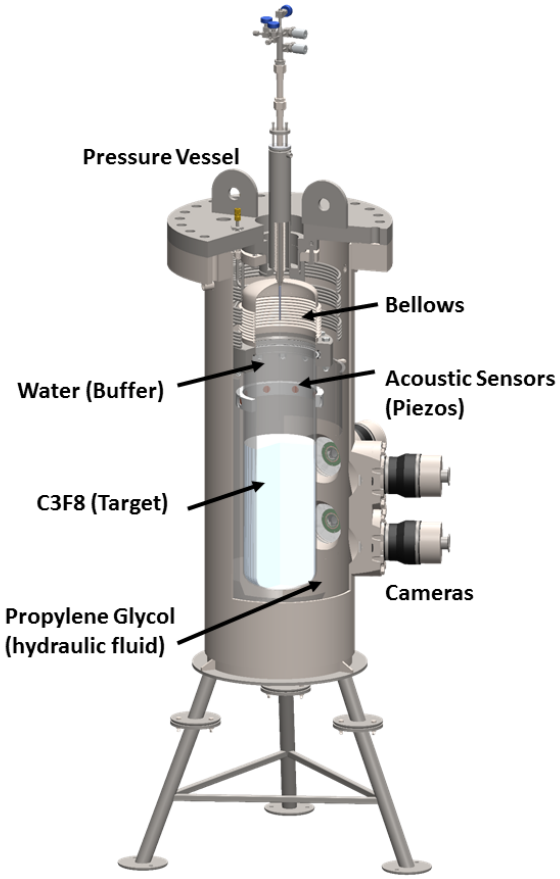

Figure 5: A schematic representation of the PICO-60 detector. The active volume is C_3F_8, operated at a temperature and pressure that characterizes a moderately superheated fluid (see Chapter 4). By setting the temperature of the surrounding water bath, the threshold is controlled. Applying pressure to the hydraulic fluid compresses/expands the bellows to control the operating conditions of the active volume. To isolate the target from the stainless steel components, a water buffer was implemented between the bellows and the C_3F_8. Primary data is collected by piezo acoustic sensors and four fast cameras.

The bubble chamber design involves a quartz jar filled with C_3F_8 and includes piezo electric acoustic transducers coupled to the glass. The unpaired proton in this fluorine rich target is optimal for the spin dependent search and offers radio-purity thanks to the fact fluorine only has one stable isotope with a natural abundance of 100%. The detector is monitored by four cameras along with pressure and temperature sensors, which allow the measurement of acoustic and optical data during bubble formation in the fiducial volume. The piezo electric transducers are fundamentally important for background suppression, because of the discovery that alpha particles generate a far louder signal than other recoil events. So the reconstruction of the acoustic parameter (AP) allows the efficient removal of alpha backgrounds from the data.

During operation, a small amount of energy deposited in the liquid will cause a transition to a gas producing a bubble (see Chapter 4). Once a reaction takes place, the detectors high pressure accumulator fires, increasing the pressure in the active volume. This effectively reverses the bubble formation and returns the detector to a fully liquid state. After a brief wait, the pressure is slowly lowered, returning the system to a meta-stable state for the next interaction.

In the search for WIMPs, the expected signal in PICO is a single bubble event. Dark matter is weakly interacting and statistically unlikely for more than one bubble to be produced by a single interacting DM particle. This is why acoustic discrimination of alpha particles is so important, because these particles create single bubbles mimicking the dark matter signal. Neutrons on the other hand are primarily identified from multiply scattering events, which are measured as several bubbles generated instantaneously (as observed by the cameras.) The process is understood as the neutron undergoing several elastic/quasi-elastic scattering events in the active volume before passing below the threshold or leaving the detector. However, this is not always the case because neutrons can generate a single bubble. These singles are problematic in the dark matter search because they're indistin-

guishable from WIMP candidates.

From a detailed analysis of simulations, a neutron singles to multiples ratio of about 1:3 is expected (see Chapter 7). This means, for every single bubble produced by a neutron there will be three multi-bubble events. By measuring the multiples and singles rate during a calibration run, it can be established if the detector is dominated by neutron interactions or if there are extra (unknown) particles producing events.

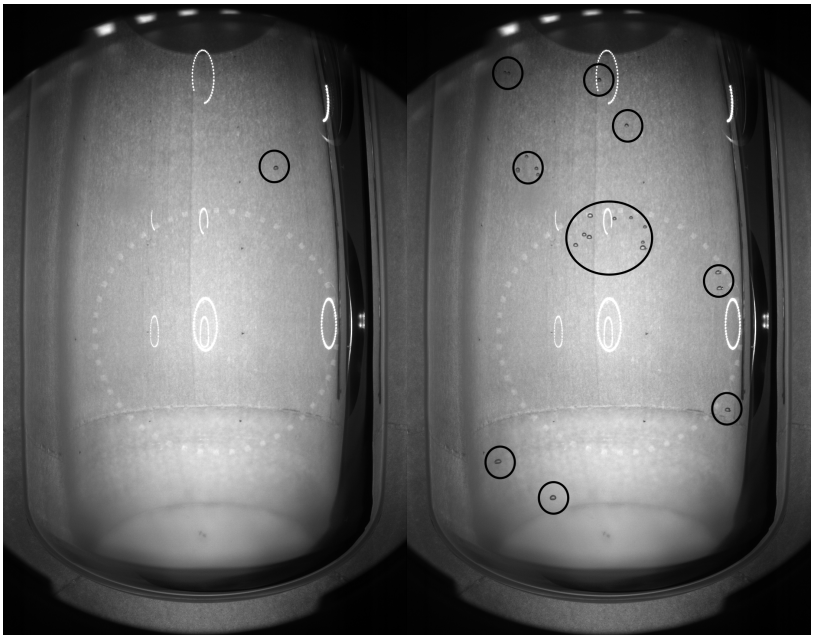

Figure 6: Example of single and multi-bubble events from neutrons in PICO-60 calibration runs, as seen by camera 1. The left image shows a single bubble event that would be indistinguishable from a dark matter candidate. The right image shows a 22 bubble event produced during a neutron calibration run.

To better understand neutron interactions in the detector, the PICO-60 mult-bubble data needs to be analyzed. The goal is to determine what information can be extracted from these events to improve background identification.

4 Dark Matter Amidst Backgrounds

In the search of new physics, the PICO detectors are constructed deep underground to be shielded from cosmogenic backgrounds [33]. The dominant background source comes from high energy particles interacting in the planet's upper atmosphere, where they can produce showers of secondary particles, like muons, that are easily measured in extremely sensitive equipment. Going deep underground provides sufficient rock overburden to prevent the majority of these secondary particles from making it into the detector, allowing clear identification of rare events. For example, SNOLAB is located 2,072 m underground which corresponds to 6010 mew (meters water equivalent.) At this depth, the average muon rate is 0.27 $\mathrm{m}^{-2}\mathrm{day}^{-1}$ [34].

Although location significantly improves background suppression, the detector materials bring along intrinsic sources that are much harder to eliminate. Most notable are the short lived alpha daughters generated by the decay of ^{222}Rn:

$$\begin{aligned} {}^{222}Rn &\rightarrow {}^{218}Po + \alpha + 5.6MeV, \\ {}^{218}Po &\rightarrow {}^{214}Pb + \alpha + 6.1MeV, \\ {}^{214}Po &\rightarrow {}^{210}Pb + \alpha + 7.8MeV. \end{aligned} \tag{1}$$

To minimize the contamination of radon in bubble chambers, the detector components need to be carefully selected to prevent an excess of alpha particles from radon. The persisting alphas can be identified and removed thanks to acoustic analysis tools, see Chapter 8, that cut out alpha backgrounds.

Additional backgrounds originate from the lab environment itself, and primarily consist of neutrons that are produced in the surrounding rock. To prevent these neutrons from being detected, PICO submerges the detector in approximately 20 tonnes of ultra pure wa-

ter (UPW). This acts to moderate lab generated neutrons, so they either don't make it to the detector or they thermalize and fall below the detectable energy threshold. Some fast neutrons originating from the detector materials remain and are primarily identified by the singles to multiples ratio.

The final background in dark matter searches are typically associated with electrons and/or gammas. These do not affect PICO, because of the energy threshold the detectors operate at. The implication is that the bubble chamber is not sensitive to the energy deposited by electrons and gammas. Therefore, to investigate the phase space accredited to WIMP candidates, it's fundamentally important to minimize the amount of radon introduced to the system and to carefully understand the detectors response to neutrons. Otherwise the discovery of new physics processes might be miss-interpreted backgrounds.

5 Extended PICO Analysis

PICO-60 was operated at SNOLAB from 2016 to 2017. During its dark matter search, no events were characterized as being consistent with the properties of dark matter [23, 24]. From the complete data set, there are calibration runs using AmBe and ^{252}Cf radioactive neutron sources that include over 3,000 single and multi-bubble events. Previously only the single bubble events were reconstructed and analyzed. The extended analysis of this data will conclude with a fit of single bubble AP values to include nuclear reactions (Chapter 8), and the 3D reconstruction of multiples in the active volume (Chapter 9).

The PICO detectors operate in a meta-stable state described by a local minimum in the Gibbs free energy [35], which is a thermodynamics potential used to model the work done to a closed system under constant pressure and temperature. PICO-60 is kept at a constant temperature that is maintained from being submerged in a water tank. The pressure is controlled using an accumulator that acts on the hydraulic fluid.

The pressure is cycled to optimized the live time when data is being collected. To start a run the hydraulic fluid, and in turn the C_3F_8, is compressed to $\approx$ 190 psia. An event begins by slowly dropping the pressure (expansion) to 30.2$\pm$0.3 psia. The result is a meta-stable state, where a small amount of energy will initiate a phase transition from a liquid to a gas (bubble nucleation).

The energy required from nuclear recoils and alpha interactions to initiate the transition is described by the Seitz threshold [36]. The basic property of the fluid is described by Equation 2:

$$P_b - P_l = \frac{2\sigma}{r_c}. \tag{2}$$

Where P_b is the vapour pressure (inside the bubble), P_l is the liquid pressure (outside the bubble), σ is the surface tension of the fluid, and r_c is the critical radius. This equation describes the pressure difference necessary, given the characteristics of the liquid, to generate a bubble that will continue to expand ($r < r_c$) and not simply collapse ($r > r_c$). Where r is the radius of the volume that the energy is deposited to.

Equation 3 gives the energy threshold, E_T, of the detector [37]:

$$E_T = \frac{4}{3} r_c^3 \rho_b \left(h_b - h_l\right) + 4\pi r_c^2 \left(\sigma - T\frac{\partial \sigma}{\partial T}\right) - \frac{4\pi}{3} r_c^3 \left(P_b - P_l\right), \tag{3}$$

Here ρ_b is the vapour density, h_b is the enthalpy of the gas, h_l is the enthalpy of the fluid, and T is the temperature of the detector. These material properties are extracted from the REFPROP [38] package. The model prescribes the pressure required, at constant temperature, to produce a visible bubble when the energy deposited within the critical radius surpasses threshold. For example, at 30.2$\pm$0.3 psia and 13.9 $\pm$ 0.1°C the threshold is 3.28 $\pm$ 0.09 keV [24].

When nucleation takes place, the detector measures the acoustic energy emitted during

bubble expansion, records images from four offset cameras along with pressure and other operational parameters. As the bubble grows, the cameras will trigger when the difference in pixel values between frames exceeds a calibrated set point consistent with motion in the detector. The trigger initiates the pressure system to compress, which reverses boiling and returns the system to a high pressure state. When the pressure reaches equilibrium, the pressure system expands for the next event.

The key analysis for the dark matter search is to report how many single bubble events took place at a specified threshold, which cannot be attributed to background sources.

5.1 Energy Reconstruction

The energy threshold of the detector describes the minimum recoil energy required to cause bubble nucleation. This means for bubble chamber events the deposited energy cannot be measured. All that can be determined is that the particles energy was above threshold. Chapter 6 presents an attempt to confirm if multi-bubble events provide enough information to reconstruct the primary energy of a neutron. The approach will study the correlation between primary neutron energy and the number of bubbles formed and the spread between bubbles in a cluster. The concept of energy reconstruction is sketched in Figure 7.

The speculation is that a higher energy neutron will generate more bubbles, as demonstrated by the 4 MeV to 6 MeV schematic presented in Figure 7. Or, higher energy neutrons could travel longer between interactions, resulting in a wider cluster with greater distances between bubbles. Demonstrated by the 6 MeV and 8 MeV visualization. Chapter 6 is focused on the topic of energy resolution. Based on the results, the topic is extended to include acoustic reconstruction.

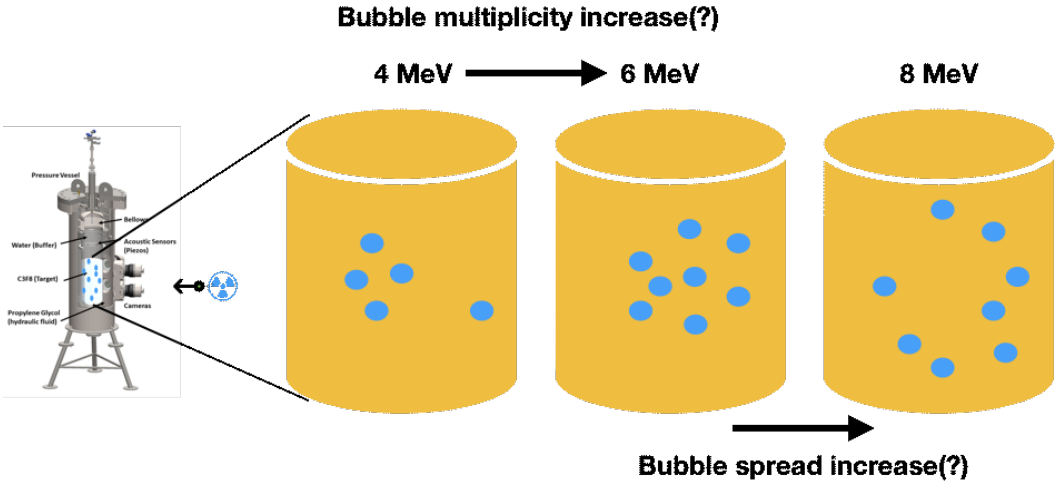

Figure 7: A sketch demonstrating the speculated observation from multi-bubble neutron events. Is there a correlation between primary neutron energy and higher multiplicity events? For example, a 4 MeV neutron generates 5 bubbles and a 6 MeV event generates 8. Otherwise, does the increase in primary energy result in a more dispersed cluster? For example, both 6 MeV and 8 MeV events generate 8 bubbles, however the later has larger distances between bubbles.

5.2 Acoustic Reconstruction

Acoustics serve a fundamental role in identifying alpha backgrounds, introduced in Chapter 4. If fast neutrons are generating single bubble events (disproving the correlation in Figure 7), the question becomes whether or not they can be identified by their acoustic parameter (AP).

AP is measured by PICO using piezo electric transducers, coupled to the quartz jars. As described in Chapter 8, the log(AP) distributions have a tail between the nuclear recoil and background alpha peaks for single bubble events. The extended analysis looks to determine if the log(AP) spectrum holds more information than previously recognized; in regards to neutron events.

The source of fast neutrons are high energy muons making it to the underground facility. They are energetic enough to cause spallation in the lab environment or detector

components, generating fast neutrons that can make it to the active volume. If these are producing single bubble events, they would be indistinguishable from dark matter unless they can be identified by measuring the acoustic signal.

5.3 Direction Reconstruction

Due to the random scattering angle of particle collisions, the exact ordering of the neutron interactions cannot be resolved as they follow a scattering pattern closely resembling a random walk. What can be questioned is whether or not the overall pattern of the bubbles point in a direction consistent with the location of the source. The idea of direction reconstruction is sketched in Figure 8.

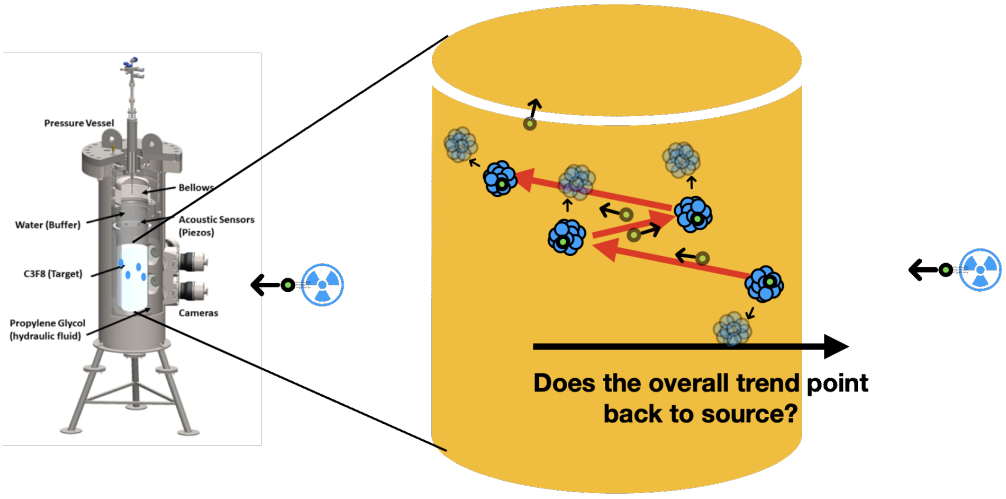

Figure 8: The exact order of neutron collisions cannot be resolved due to the random walk of neutrons in matter. Any sequence of the above collisions shown could take place. The goal is to determine if the overall bubble pattern points back to source, shown here.

From Figure 8, each point where the neutron scatters with a heavier nucleus, a bubble is formed. The exact ordering of collisions could be any sequence not illustrated, but the random nature is shown as the neutron could be scattering backwards and/or forwards. If the pattern of the four bubbles is approximated by a line, the goal is to determine if the

direction of this straight line is pointing to the source location. If true, this could help identify unknown backgrounds in the detector.

The opposite case is that the overall trend reveals nothing of the sources location. Instead of pointing back to the source, the events point off in a random direction, which offers no insight to the background. (This is addressed in Chapter 9.)

6 Neutron Reactions in Superheated C_3F_8

GEANT4 [39] was used to study neutron interactions in the bubble chamber volume. In this section, the simulated geometry is simplified to investigate the presumed correlation between neutron energy and bubble multiplicity/spread.

6.1 Energy Simulation

The naive expectation is the more energy a neutron has, the greater the potential to scatter several more times before falling below threshold. This would result in a linear relationship between the bubble multiplicity and the primary energy of the neutron. Conversely, a neutron at higher energy could pass farther into the material before reacting, resulting in greater spread between bubbles in a cluster. These intuitive predictions are consistent with the description of mean free path, which describes the scattering of particles through a medium.

The simulated geometry involved a cylindrical tank of liquid C_3F_8. The dimensions chosen ensure that 99.94% of the bubbles produced are created inside the volume: 6 meters high and 3 meters in radius, centered at (0,0,0). The neutrons are released at the center and directed towards the positive z axis. Figure 9 shows the distance of each bubble to the sources location at the origin, indicating that 99.97% of the contained bubbles are within 2 meters of the source.

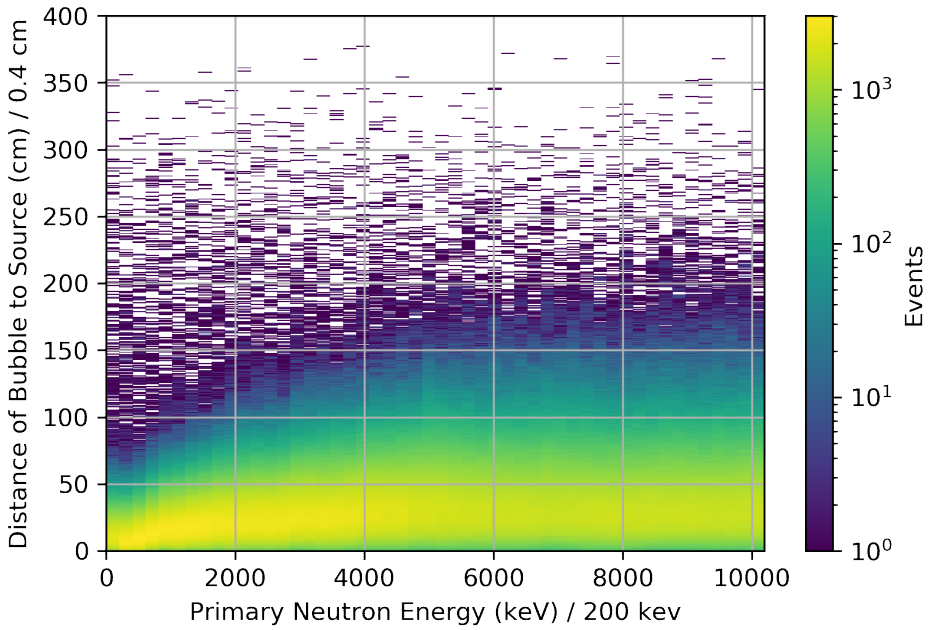

Figure 9: 2D log distribution showing the distance of every bubble to the source's location at the origin of the C_3F_8 tank, as a function of the primary neutron energy. This illustrates that 99.97% of the contained bubbles are produced within 2 meters of the source.

The neutrons simulated within the tank had primary energies ranging from 200 keV to 10 MeV, in steps of 200 keV. They are split up into 50 separate simulations, each with 10,000 primary neutrons simulated at the same energy. In Figure 9 the horizontal axis is binned with respect to the 50 simulations. The vertical axis bins the distance of every bubble to the sources location, in steps of 0.4 cm. For example, a 600 keV neutron produces a cluster of 4 bubbles. The distance of each bubble to the source is calculated and every value is binned on the vertical axis, with respect to the 3rd horizontal bin corresponding to 600 keV. The result indicates the bubbles are primarily contained within 2 meters of the source in the C_3F_8 volume being simulated.

Fully contained neutrons are not expected in PICO-60 due to the smaller dimensions of the quartz jar, which has an active region roughly 30 cm in diameter and 64 cm in height.

Without a larger detector, a fast neutron can leave the active volume before depositing enough energy to fall below threshold. How this might affect energy correlation will be discussed in the following sub-section.

The total recoil energy deposited per event is presented in Figure 10. As before, the horizontal binning corresponds to the 50 simulations, but now the vertical bins are obtained by adding the recoil energy given to each bubble per event.

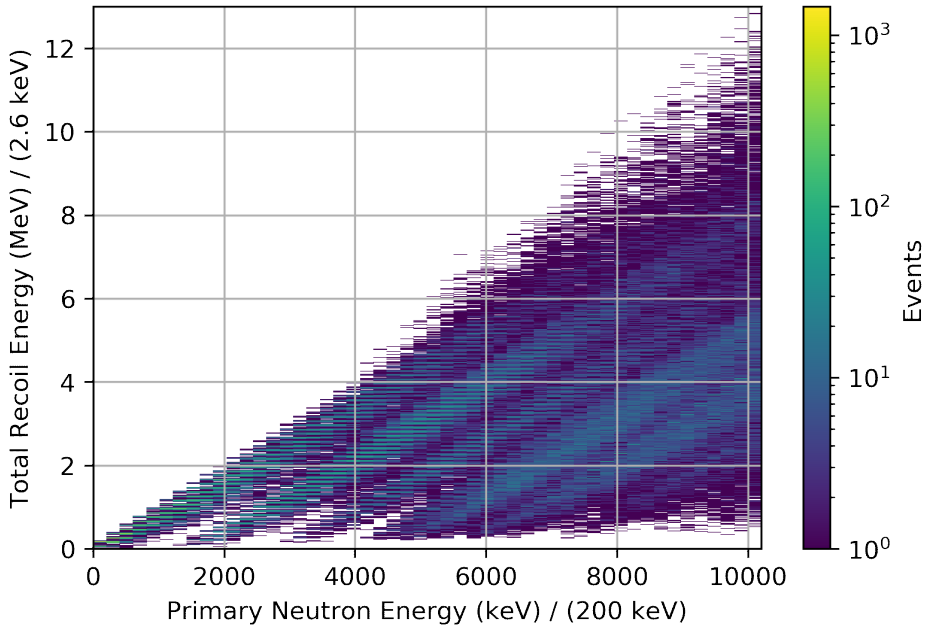

Figure 10: The total recoil energy deposited per event is determined by adding the recoil energy of every nucleus producing a bubble in the cluster. This total is binned with respect to the primary energy of the neutron. The 2D log distribution shows that at higher energies, for example 8 MeV, the neutron can undergo nuclear reactions. This is evident by some events depositing more recoil energy then the neutron started with, and by the events depositing significantly less energy than the primary neutron. The linear features indicate collision channels with carbon and fluorine.

The result in Figure 10 is a series of linear features highlighting different scattering processes the neutron can undergo before falling below threshold. These features are not surprising, because the neutron will continuously scatter off ^{12}C and ^{19}F depositing a dif-

ferent amount of recoil energy every time. If the recoil energy is less than the threshold, it won't be included in the total recoil energy deposited. A striking feature of this distribution is observed at energies larger than 4 MeV, where the neutrons appear capable of depositing more energy into the C_3F_8 then they started with. For example, at 4 MeV the neutrons are depositing at most 4 MeV of total recoil energy; however at 8 MeV, there are events with more than 8 MeV of total recoil energy deposited. The explanation is that exothermic nuclear processes can deposit more energy than recoils from elastic/quasi-elastic scattering.

6.2 Neutron Reactions

To check how nuclear reactions affect bubble multiplicity, the bubble multiplicity per event is shown with respect to primary neutron energy in Figure 11. Also included are the profile distributions for the contributing reactions, labelled according to the reaction channel (full list of reactions are summarized in Tables 1, 2, and 3). To simplify notation, (n,α) will be used to identify nuclear reactions with outgoing alpha particles. Similarly, (n,^{x}H) will identify reactions with hydrogen nuclei emitted.

The ^{19}F and ^{12}C recoils show identical profile distributions because these multi-bubble events include neutron scattering off both elements. The first bubble GEANT4 generates classifies the event as being a carbon or fluorine recoil. On the other hand, the ^{19}F(n,α+n)^{15}N reaction produces a secondary neutron that continues on to scatter with ^{19}F and ^{12}C. Therefore, multi-bubble events are identified by first checking nuclear reactions; if found the multi-bubble event is classified by the nuclear reaction, otherwise the event is classified by the first recoil (^{19}F or ^{12}C).

Figure 11 hints that before 1.5 MeV there is a linear relationship between bubble multiplicity and primary neutron energy, from nuclear recoils with carbon and fluorine. This immediately breaks down as the energy increases further. Considering the energy scale of

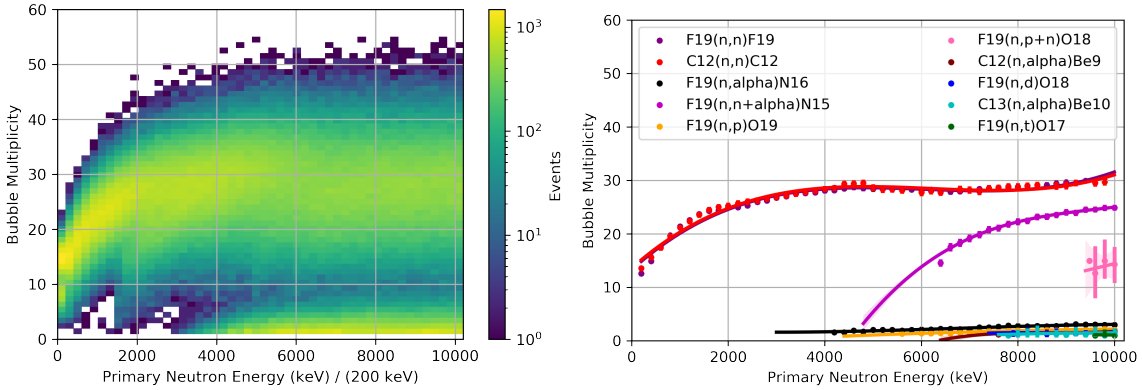

Figure 11: The 2D histogram summarizes the bubble multiplicity observed for mono-energetic neutrons in GEANT4, depending on the primary neutron energy. The distribution indicates a linear increase in bubble multiplicity for energies below 1.5 MeV, followed by an increase in single bubble events and a saturation of high multiplicity events. Included are profile distributions for the contributing reactions. The high multiplicity events are primarily associated with nuclear recoils with ^{19}F and ^{12}C. The low multiplicity events are coming from (n,α) and (n,^{x}H) type reactions. The ^{19}F(n,n+α)^{15}N and ^{19}F(n,n+p)^{18}O channels contribute to high multiplicity events because the secondary neutron is above threshold.

the primary neutrons, it's evident that nuclear reactions are taking place. This explains the excess energy noted earlier in Figure 10 and clarifies the sudden increase of single bubble events in Figure 11 at higher energies.

The source of single bubble events come from (n,α) and (n,^{x}H) type reactions, which are depositing all outgoing kinetic energy at one location, causing a single bubble to nucleate. A full list of possible neutron reactions at these energies and target fluid is summarized in Tables 1, 2, and 3 [40]. The tables highlight the percentage of each process being observed using energy simulations 2, 4, 6, 8, and 10 MeV. Each column represents the reactions for 10,000 primary neutrons simulated in the tank geometry.

From the tables, the Q-value for ^{19}F(n,α)^{16}N reactions explains the 1.5 MeV threshold observed in the figures. Primary neutrons above this energy are now able to undergo nuclear reactions.

C_3F_8 World: Percentage of Neutron Reactions at Respective Energies						
Reaction	Q-value (MeV)	2 MeV (%)	4 MeV (%)	6 MeV (%)	8 MeV (%)	10 MeV (%)
$^{19}F(n,n)^{19}F$	0	76.01	75.33	74.74	73.90	73.43
$^{19}F(n,\alpha)^{16}N$	-1.525	-	0.11	0.79	0.71	0.53
$^{19}F(n,\alpha+n)^{15}N$	-4.014	-	-	0.09	0.76	1.59
$^{19}F(n,p)^{19}O$	-4.038	-	-	0.08	0.21	0.18
$^{19}F(n,d)^{18}O$	-5.769	-	-	-	0.05	0.03
$^{19}F(n,p+n)^{18}O$	-7.994	-	-	-	-	0.01
$^{19}F(n,t)^{17}O$	-7.557	-	-	-	-	0.01
$^{12}C(n,n)^{12}C$	0	23.99	24.56	24.30	24.14	23.98
$^{12}C(n,\alpha)^{9}Be$	-5.702	-	-	-	0.18	0.23
$^{13}C(n,\alpha)^{10}Be$	-3.836	-	-	-	0.05	0.01

Table 1: Summary of the possible reactions neutrons with MeV range energies can initiate in the target fluid. Each column represents 10,000 primary neutrons simulated into the tank of C_3F_8 geometry, leading to 238,440 interactions at 6 MeV. The percentages include every bubble produced and is not limited to individual events: a 6 MeV neutron generating 10 bubbles will contribute 10 reactions to the percentages in the 6 MeV column. The main reaction is the elastic/quasi-elastic scattering of neutrons off carbon and fluorine. As the primary energy exceeds 1.5 MeV, nuclear processes become possible.

The percentages in Table 1 include all the reactions generating bubbles. For example, a 6 MeV neutron could generate a cluster of 10 bubbles that includes 2x ^{12}C, 7x ^{19}F, 1x α and ^{16}N recoils, contributing 10 reactions to the percentages in the 6 MeV column, (assuming α and ^{16}N are indistinguishable). As anticipated, the majority of bubbles are created by elastic scattering of neutrons with ^{19}F and ^{12}C. However, as the energy increases past 1.5 MeV the number of nuclear reactions starts to increase (see Chapter 7 for cross sections).

C_3F_8 World: Percentage of Single Bubble Neutron Reactions at Respective Energies						
Reaction	Q-value (MeV)	2 MeV (%)	4 MeV (%)	6 MeV (%)	8 MeV (%)	10 MeV (%)
^{19}F(n,n)^{19}F	0	0.01	-	0.02	-	-
^{19}F(n,α)^{16}N	-1.525	-	1.72	8.14	4.23	2.89
^{19}F(n,α+n)^{15}N	-4.014	-	-	0.03	0.03	0.05
^{19}F(n,p)^{19}O	-4.038	-	-	0.86	1.49	1.67
^{19}F(n,d)^{18}O	-5.769	-	-	-	0.06	0.4
^{19}F(n,p+n)^{18}O	-7.994	-	-	-	-	-
^{19}F(n,t)^{17}O	-7.557	-	-	-	-	0.09
^{12}C(n,n)^{12}C	0	-	-	-	0.01	-
^{12}C(n,α)^{9}Be	-5.702	-	-	-	2.2	2.75
^{13}C(n,α)^{10}Be	-3.836	-	-	-	0.03	0.05

Table 2: Percentage of reactions generating single bubble events. At 2, 6, and 8 MeV the ^{19}F(n,n)^{19}F and ^{12}C(n,n)^{12}C reactions are n-capture, which are grouped under nuclear recoils because the energy deposited is indistinguishable. All remaining single bubble events in the table are the result of (n,α) or (n,^{x}H) reactions, consistent with Figure 11.

Tables 2 and 3 are different from Table 1, because they show the percentage of reactions observed per event (consistent with the profile distributions shown in Figure 11). Table 2 (3) shows only single (multi-) bubble events. The percentages in each column add to 100% by adding both table columns together. For example, at 2 MeV 99.99% of the reactions are multi-bubble events and 0.01% are singles. From Figure 2, the single bubble events with carbon (see 8 MeV) and fluorine (see 2 and 6 MeV) are actually n-capture events; after the collision the nuclei are excited and then de-excite via γ emission, which goes undetected. These reactions aren't discussed in detail, because the recoil energy associated with them are indistinguishable from nuclear recoils.

C_3F_8 World: Percentage of Multi-Bubble Neutron Reactions at Respective Energies						
Reaction	Q-value (MeV)	2 MeV (%)	4 MeV (%)	6 MeV (%)	8 MeV (%)	10 MeV (%)
^{19}F(n,n)^{19}F	N/A	84.72	68.18	61.23	42.04	30.52
^{19}F(n,α)^{16}N	-1.525	-	1.06	9.6	10.8	8.13
^{19}F(n,α+n)^{15}N	-4.014	-	-	1.59	16.22	36.80
^{19}F(n,p)^{19}O	-4.038	-	-	0.33	1.82	2.26
^{19}F(n,d)^{18}O	-5.769	-	-	-	0.04	0.23
^{19}F(n,p+n)^{18}O	-7.994	-	-	-	-	0.13
^{19}F(n,t)^{17}O	-7.557	-	-	-	-	-
^{12}C(n,n)^{12}C	N/A	15.27	29.04	18.2	20.17	11.41
^{12}C(n,α)^{9}Be	-5.702	-	-	-	0.85	2.60
^{13}C(n,α)^{10}Be	-3.836	-	-	-	0.01	0.02

Table 3: Percentage of reactions generating multi-bubble events. The primary channel are (elastic) nuclear recoils of ^{19}F and ^{12}C. Events with α, deuterium, or proton particles emitted are primarily low multiplicity events where the neutron first scattered off carbon/fluorine before undergoing the nuclear reaction. Events emitting neutrons generate a high multiplicity, because these neutrons are above threshold and continue scattering after undergoing the nuclear reaction.

The conclusion from Tables 2 and 3 is that single bubble events in the tank geometry are overwhelmingly the result of nuclear reactions. The simulation indicates that elastic nuclear recoils with carbon and fluorine only produce high multiplicity events. Multi-bubble events involving (n,α) reactions have low multiplicity and are produced by the neutron first undergoing nuclear recoils with carbon and fluorine. When multi-bubble (n,^{x}H) reactions take place, the energy of the secondary neutron is always below 1.5 MeV, but above 3.3 keV. Therefore, a multi-bubble event never includes more than one nuclear reaction, the remaining bubbles involve nuclear recoils with ^{19}F and ^{12}C.

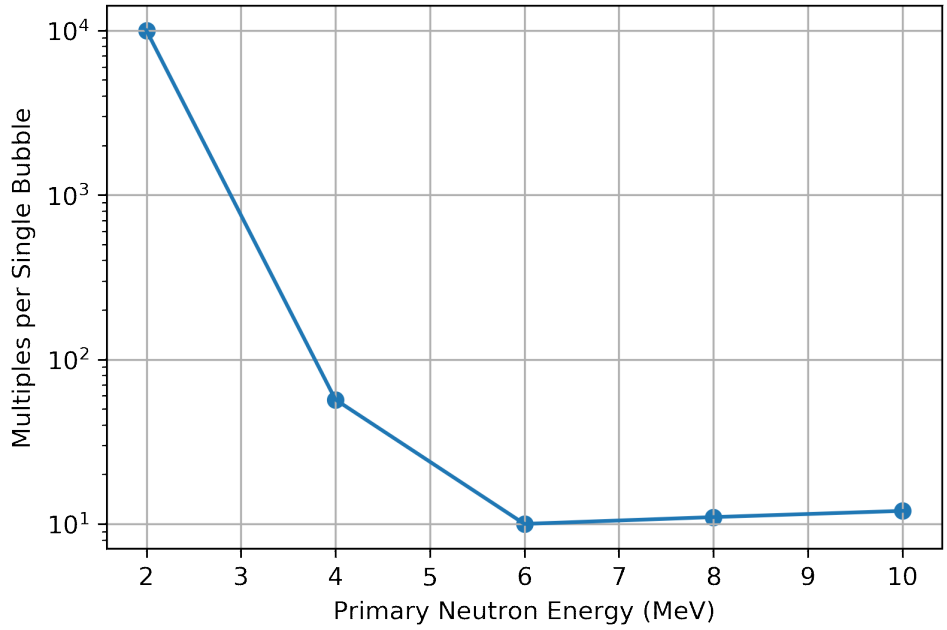

Figure 12: Number of multi-bubble events expected per single bubble in the GEANT4 tank geometry. This does not follow the 1:3 singles to multiples ratio, which is expected because the source is embedded in the C_3F_8 volume.

The deviation from the 1:3 singles to multiples ratio expected from neutrons (introduced in Chapter 3) is not surprising, because of the choice in geometry. The number of multi-bubble events per single bubble, from Tables 2 and 3, is shown in Figure 12. With the source placed within the C_3F_8 tank, the neutron starts off with the primary energy and therefore scatter continuously in the large volume. For the PICO-60 geometry (see Chapter 7), the fluorine and carbon multiplicities should be less because the neutron will loose energy before reaching the detector (plus the neutron's energy might not be fully contained). Containment however proves to not be the limiting factor in reconstructing primary neutron energy. The observation of single bubble events from fast neutrons means there is no linear relationship between bubble multiplicity and primary neutron energy, irrelevant of the detector size.

This leaves energy reconstruction to the spread between bubbles in a cluster. This anal-

ysis first calculates the center of gravity, $\vec{\xi}$, for an event using:

$$\vec{\xi} = \frac{1}{N}\left(\sum_{i=1}^{N} x_i, \sum_{i=1}^{N} y_i, \sum_{i=1}^{N} z_i\right). \tag{4}$$

Where N is the total number of bubbles in the cluster, and (x,y,z) are the individual bubble coordinates.

The average distance of every bubble in the cluster to $\vec{\xi}$ is calculated and represented on a 2D histogram in Figure 13, including the profile distribution overlaid. The average distance between bubbles in a cluster saturates at energies above 1.5 MeV. Therefore, the spread of multi-bubbles from the center of gravity does not offer enough information to reconstruct the primary neutron energy.

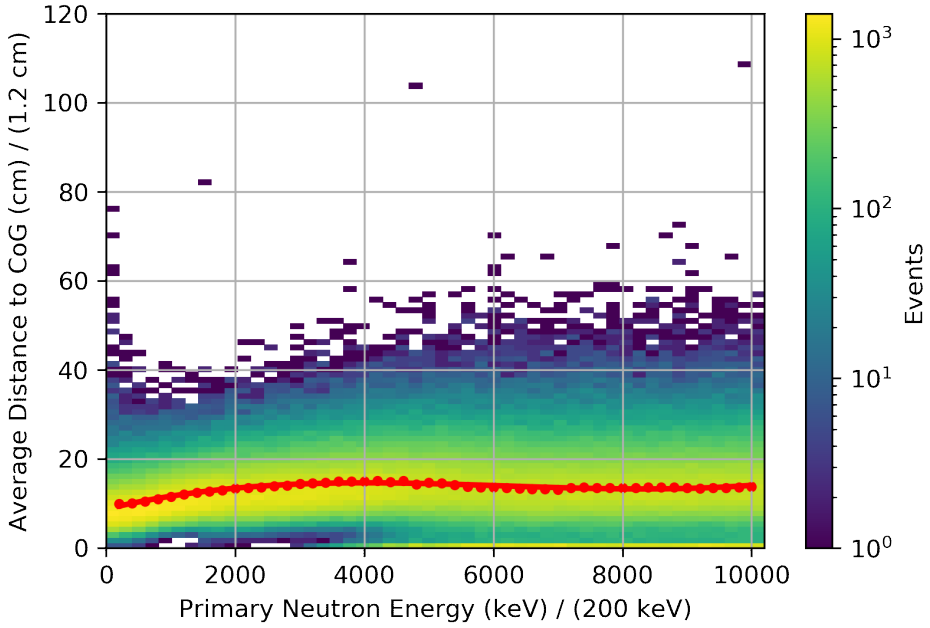

Figure 13: 2D distribution showing the average distance of each bubble to the center of gravity (CoG). The red curve shows the profile distribution where the error bars are too small to be observed. It can be seen that the average spread between bubbles in a cluster does not increase with energy.

Although direct energy reconstruction based on bubble multiplicity or cluster size breaks down above 1.5 MeV, the acoustic power of these single bubble nuclear reactions might allow energy reconstruction. Using the PICO-60 detector geometry, the number of nuclear recoils observed during a calibration run can be extracted if (n,α) and (n,^{x}H) reactions are distinguishable in the AP spectrum.

7 Simulating the PICO-60 Geometry

The previous geometry was simplified to a large cylinder of C_3F_8 to study the type of reactions expected from neutrons in the detector fluid. The energy range and number of neutrons simulated was arbitrary to focus on the relationship between bubble multiplicity and energy. To get a realistic picture of how neutron interact in the detector, the simulation needs to mimic the geometry and operating conditions of PICO-60.

7.1 Cross Sections: Neutron Reactions

The reaction probability is characterized by the reaction cross sections, as described in Chapter 2. Unlike dark matter, the neutron cross sections are very large and are provided in Figures 14 and 15.

The cross sections in Figure 14 are for all the nuclear reactions that can take place in C_3F_8 from neutrons, (see Tables 1, 2, and 3). Figure 15 shows the cross sections for the elastic scatter of neutrons with ^{19}F and ^{12}C. The cross sections come from the Evaluated Nuclear Data File (ENDF) [41] and the Joint Evaluated Fission and Fusion File (JEFF) [42]. These cross section data bases are directly referenced by the GEANT4 toolkit. The natural abundance of ^{13}C (about 1.1%) is also modelled in GEANT4, which explains the appearance of ^{10}Be.

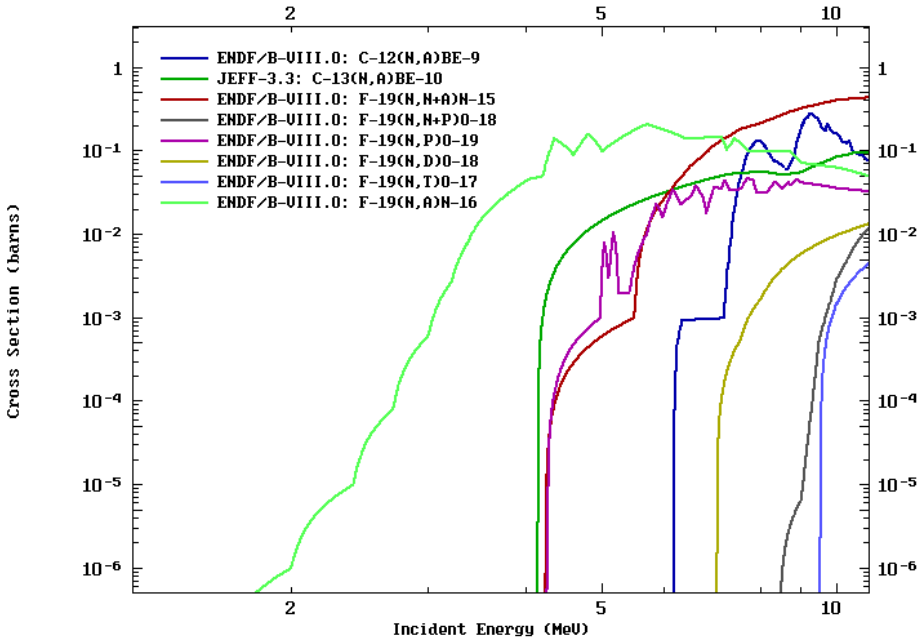

Figure 14: Neutron induced nuclear reactions in C_3F_8. Geant4 uses the ENDF/B-VII [41] and JEFF [42] databases. The natural abundance of ^{13}C is included in GEANT4, resulting in the dark green curve. Tables 1, 2, and 3 summarize all reactions.

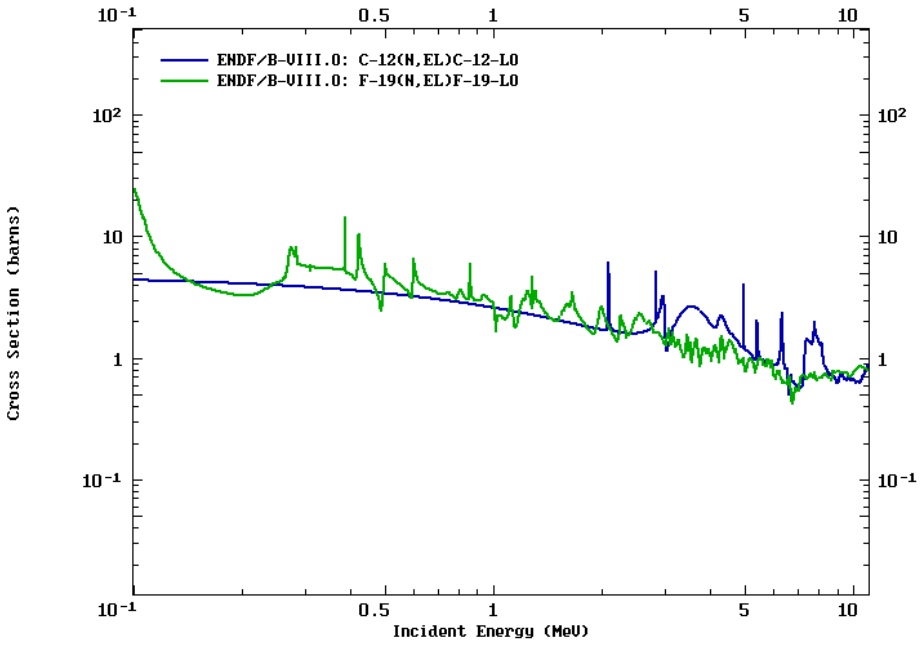

Figure 15: Neutron cross sections for elastic scatter with ^{19}F and ^{12}C. Geant4 uses the ENDF/B-VII [41] database.

7.2 Detector Components

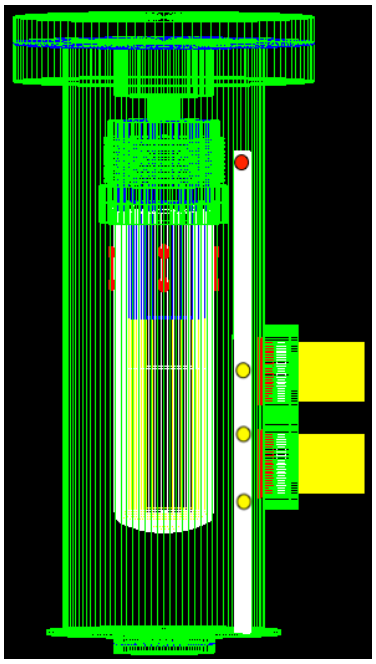

Figure 16: The PICO-60 geometry as modelled in GEANT4. Radioactive sources are placed within the white cylinder to mimic deployment during the calibration runs. The red circle represents the AmBe source: 144.0 $\pm$ 2.5 cm above the bottom of the source tube. The yellow circles represents different placements of the ^{252}Cf source: 40.0 $\pm$ 2.5 cm, 60.0 $\pm$ 2.5 cm, and 80.0 $\pm$ 2.5 cm above the bottom of the source tube. Key components of the geometry are: Blue, water buffer liquid. Green, stainless steel (note the source tube is located outside of the pressure vessel). White vessel, quartz jar. Light yellow, C_3F_8. Red, piezo transducers and cables. The empty space between the quartz jar and pressure vessel is filled with hydraulic fluid (propylene glycol).

To model the reactions expected in PICO, neutron simulations were conducted using a geometry representative of the PICO-60 detector, see Figure 16. The main components influencing the neutron propagation are visible in the image, while additional components are not shown to improve visibility (for example, the retro-reflector and water tank). To compare with calibration data, the neutrons are emitted isotropically from the four source locations shown in the image using coloured circles. The ^{252}Cf source was placed at the three positions marked by yellow circles (40.0 $\pm$ 2.5 cm, 60.0 $\pm$ 2.5 cm, and 80.0 $\pm$ 2.5

cm above the bottom of the source tube) and the AmBe source was placed at the red circle (144.0 ± 2.5 cm above the bottom of the source tube). These positions represent the placement of the sources in the PICO-60 calibration data.

The long white cylinder is representative of the source tube that is located outside of the pressure vessel. The radioactive sources are fed down the tube to be in close proximity with the detector. The green components are stainless steel. The white inner component is the quartz jar of the detector, where the space between the jar and the pressure vessel is filled with propylene glycol (not shown for clarity). The C_3F_8 volume is shown in light yellow within the white quartz jar. Blue is the water buffer liquid that isolates the active volume from the stainless steel components. Red indicates piezo locations and cables, and finally dark yellow are the camera enclosures. Shown here are two cameras, but the complete detector has four. The two missing cameras would block the view of the detector in this image, as the source tube is located between the two camera columns.

These components, aside from the camera enclosures, are required in the simulation, because neutrons generated at the source tube must travel through the different layers before reaching the target fluid. Some of the neutron energy will be lost on the way and a significant fraction of neutrons won't make it to the active volume.

7.3 Performance

To replicate neutron production from AmBe and ^{252}Cf sources, the random generator in GEANT4 is configured to fire neutrons isotropically, centered at the locations specified in Figure 16. This mimics calibration data taking, because in a source there is no control over neutron direction. The energy of each neutron is generated by randomly drawing values using energy probability distributions for AmBe [43] and ^{252}Cf [44, 45]. For example, the energy distribution of 10,000 random neutrons from each source is shown in Figure 17.

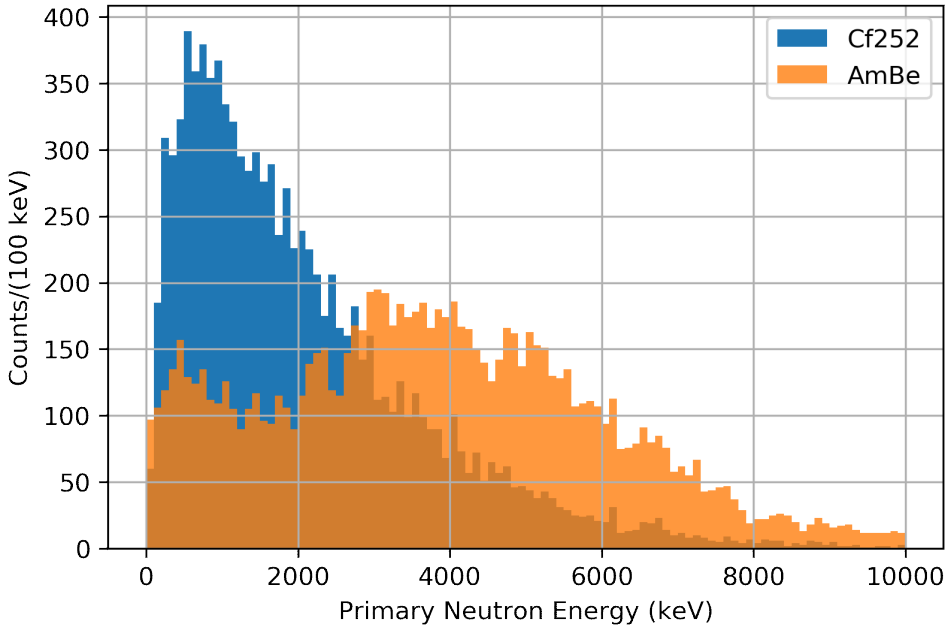

Figure 17: Neutron energy distributions for AmBe (orange) and ^{252}Cf (blue). Shown are 10,000 primary neutrons simulated for each source based on probability distributions [43, 44, 45]. To simulate neutrons in the PICO geometry, a neutron is simulated istropically in the source tube with an energy randomly drawn using these distributions.

The total number of primaries simulated that reacted with the target, along with the respective number of singles/multiples, is summarized in Table 4. These locations mimic the real deployment used for the calibration runs. The source position was defined by placing the source at the very bottom of the tube and then retracting the source to the respective distance (with a positioning uncertainty of 1 inch).

As anticipated, a significant number of neutrons generated never make it into the detector (over 1 billion AmBe neutrons are simulated, and 35 million are simulated for each Cf source placement). The energy distribution of primary neutrons that do reach the detector is shown in Figure 18. In comparison to the distribution shown in Figure 17, Figure 18 shows that only higher energy neutrons are able to create secondaries above threshold, as expected because the neutrons loose energy before reaching the target volume.

PICO-60 Geometry Neutron Simulations			
Source (± 2.5 cm)	Total (± 800)	Singles (± 0.2 %)	Multiples (± 0.2 %)
AmBe (144 cm)	46,398	32.3	67.7
^{252}Cf (40 cm)	270,193	27.7	72.4
^{252}Cf (60 cm)	344,250	25.5	74.5
^{252}Cf (80 cm)	313,114	26.9	73.1

Table 4: Summary of neutron events from each source using the PICO-60 geometry, (see Figure 16). The locations were chosen to replicate calibration runs. 1,003,735,647 primary neutrons are simulated for AmBe, and 35 million are simulated for each Cf source.

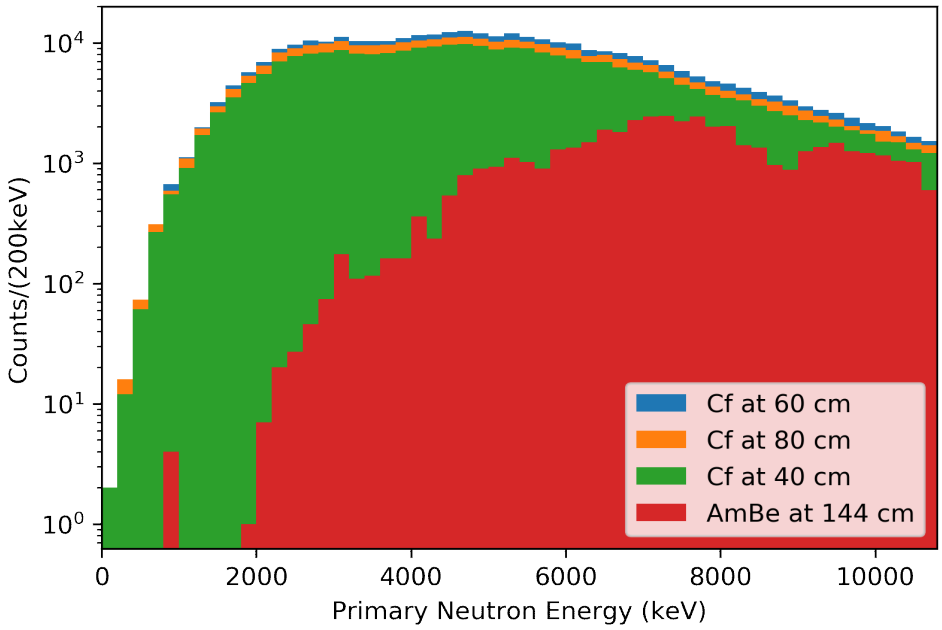

Figure 18: Distribution of primary neutrons that make it into detector for each source type and placement.

The energy of the neutron as it enters the detector is shown in the sub plots of Figure 19. These figures present the respective distributions for the four source locations. Blue (red) is the energy of every neutron entering the detector that produces a single (multi-) bubble event. Orange shows the energy of neutrons generating a single bubble (n,α) type reaction, and similarly green shows that for the (n,^{x}H) type reactions.

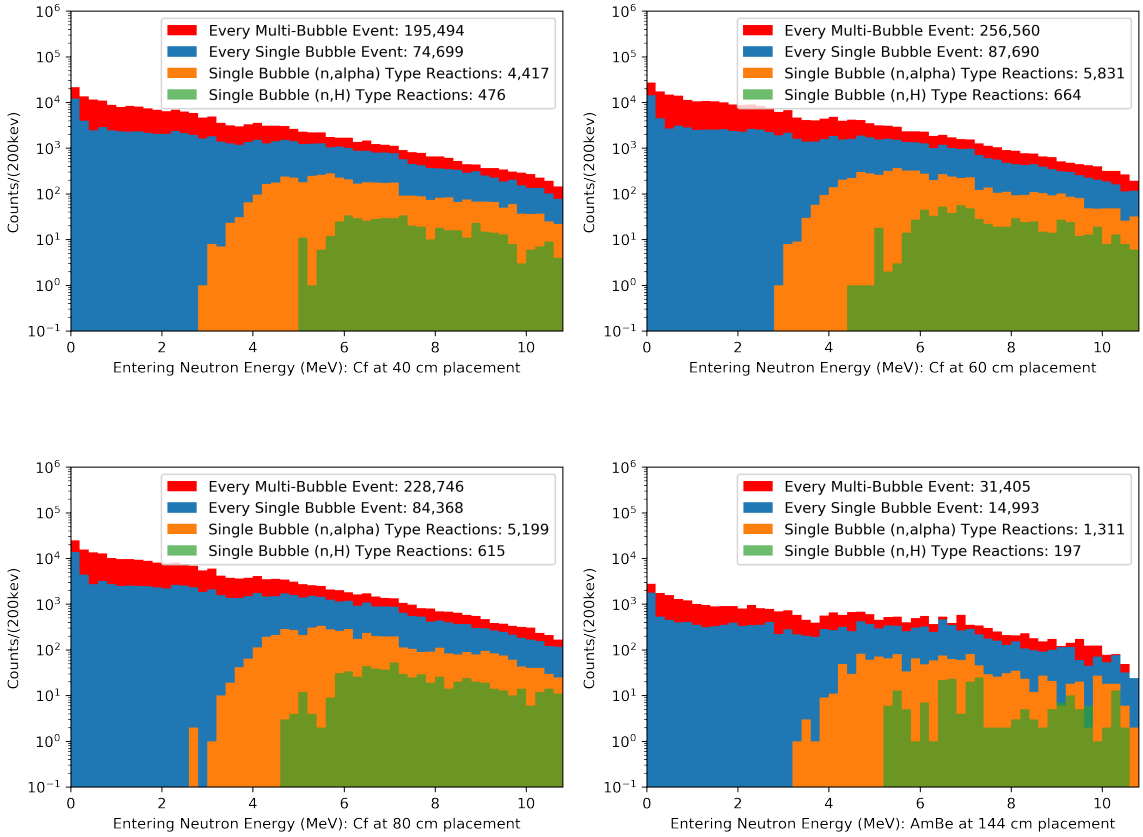

Figure 19: Distributions for each source type/placement showing the energy of the neutron as it enters the active volume to produce a single bubble event. Blue shows all interacting neutrons creating a single bubble, orange shows only single bubble (n,alpha) type reactions, and green shows the single bubble (n,^{x}H) type reactions. For comparison, red shows the neutron energy as it enters the active volume to produce a all multi-bubble event.

Figure 19 demonstrates that the energy of the neutrons generating nuclear type reactions are all greater than 1.5 MeV, which is consistent with the simulation of the tank of C_3F_8. Furthermore, although higher energy neutrons are making it to the detector (see Figure 18) they are losing energy before reaching the target fluid. A complete overview of the simulations is summarized in Tables 5, 6, 7, and 8.

The percentages in Tables 5, 6, 7, and 8 are obtained by counting the number of each reaction observed in the simulation and comparing to the total. The uncertainty comes from

the ^{252}Cf and AmBe placement in the source tube, for example 60.0 $\pm$ 2.54 cm. Repeating the simulations with the source raised (62.54 cm) and lowered (57.46 cm) returns an estimate for the rate uncertainties. For example, from the 60 cm placement of ^{252}Cf the recorded number of single bubble ^{19}F(n,α)^{16}N reactions is 4,947. Moving the source up and down, the rate is 4,858 and 4,912 respectfully. The standard deviation between these three simulations is 37 counts, so the rate is given as 4,947 $\pm$ 37.

The total single bubble NR, (n,α), and (n,^{x}H) type reactions are the sum of individual processes counted. For example, at 60 cm the counted reactions are: 4,947 $\pm$ 37 ^{19}F(n,α)^{16}N, 574 $\pm$ 19 ^{19}F(n,α+n)^{15}N, 309 $\pm$ 21 ^{12}C(n,α)^{9}Be, and 1 $\pm$ 4 ^{13}C(n,α)^{10}Be. Added together the total (n,α) count is 5,831 $\pm$ 47. Taking the percentage of individual rates to the total, the values in Table 6 are calculated: for example, 84.8 $\pm$ 0.9 % of the (n,α) reactions counted involved ^{16}N. The multi-bubble percentages are obtained in the same manner, however in these cases there are also ^{12}C and ^{19}F recoils taking place. The event is counted as (n,α) or (n,^{x}H) if a nuclear reaction is counted amongst the usual ^{19}F and ^{12}C recoils.

The final rate of NR, (n,α), and (n,^{x}H) reactions are added together to get the total counted singles and multiples. For example, the single bubble rates at 60 cm are: 81,195 $\pm$ 535 NR, 5,831 $\pm$ 47 (n,α), and 664 $\pm$ 15 (n,^{x}H). Added together, the total is 87,690 $\pm$ 537. Therefore, the single bubble events include 92.6 $\pm$ 0.8 % NR, 6.65 $\pm$ 0.07 % (n,α), and 0.76 $\pm$ 0.02 % (n,^{x}H). The rate of multiples are found in the same way, resulting in a count of 256,560 $\pm$ 542 events. The combined rate of singles and multiples where shown in Table 4: 344,250 $\pm$ 800 total where 25.5 $\pm$ 0.2 % are singles and 74.5 $\pm$ 0.2 % are multiples.

Included near the end of Tables 5, 6, 7, and 8 is a summary of counted single and multi bubble events from the PICO-60 calibration data. This rate and live time is determined by applying fiducial volume, data quality, and run type cuts to the full data set, see Appendix

A. Using the corresponding live time and neutron yield, the rate observed experimentally is calculated to compare with the prediction from simulation.

For example, 344,250 $\pm$ 800 of 35 million neutrons make it into the detector for the 60 cm placement of ^{252}Cf. Therefore, only 0.984 $\pm$ 0.002 % of the emitted neutrons reached the target volume with energy above threshold. If 8.72 $\pm$ 0.08 neutrons are emitted every minute (see Appendix B) and the detector is live for 5,214 $\pm$ 8 minutes, the simulation predicts a total of 447 $\pm$ 4 neutron events; 114 $\pm$ 1 singles and 333 $\pm$ 3 multiples.

The singles to multiples ratio at these source positions offers a performance check to the data set. The agreement between simulated and observed ratios for the 60 and 80 cm placement is within 1σ. The disagreement for the 40 cm and AmBe runs is at the 2σ and 4σ level respectfully. This disagreement for the sources placed lower/higher in the calibration tube needs to be investigated further.

The last section of Tables 5, 6, 7, and 8 use the percentages to determine how many single bubbles from the data are expected to fit under each reaction type. However, the calculation first requires an estimate for the number of background alpha events anticipated from the decay of ^{222}Rn. The radon α contamination in PICO-60 is known to be 0.23 μBq/kg (2.9 $\pm$ 0.3 events/live day) [24]. With a live time of 5,213 $\pm$ 8 minutes and a detector volume of 48.9 kg, the anticipated ^{222}Rn background is 3.5 $\pm$ 0.4 decays, which corresponds to 11 $\pm$ 1 alphas.

PICO-60 observed 205 $\pm$ 14 single bubble events during the 60 cm calibration run, where 11 $\pm$ 1 are expected to be background alphas. This means 194 $\pm$ 14 are neutron events. Scaling the neutron rate to the simulated percentages, 180 $\pm$ 13 are expected to be nuclear recoils, 13 $\pm$ 1 are (n,α) and 1.5 $\pm$ 0.1 are (n,^{x}H) type reactions.

The simulation results predict that nuclear reactions can be accounted for in the calibration runs. Knowing these events could exist in the data, the next question is if they can be distinguished in the AP distribution.

^{252}Cf – 40 ± 2.4 cm from bottom of source tube		
Reaction Type	Single Bubble (%)	Multiple Bubbles (%)
Nuclear Recoil	93 ± 1	97.5 ± 0.6
(n,α)	5.91 ± 0.08	2.37 ± 0.04
(n,^{x}H)	0.64 ± 0.02	0.12 ± 0.01
^{19}F(n,α)^{16}N	84 ± 1	45 ± 1
^{19}F(n,α+n)^{15}N	10.7 ± 0.4	53 ± 2
^{12}C(n,α)^{9}Be	5.0 ± 0.5	1.94 ± 0.07
^{13}C(n,α)^{10}Be	0.07 ± 0.09	-
^{19}F(n,p)^{19}O	96 ± 4	92 ± 13
^{19}F(n,d)^{18}O	4 ± 2	5 ± 1
^{19}F(n,n+p)^{18}O	-	1.7 ± 0.4
^{19}F(n,t)^{17}O	-	0.9 ± 0.4
PICO-60 Data – Run Type 14: Singles to Multiples 48 ± 6 %		
Live Time (min)	Single Bubble	Multiple Bubbles
2617 ± 3	103 ± 10	205 ± 14
Prediction from Simulation: Singles to Multiples 38.0 ± 0.5 %		
Neutron Yield	Singles	Multiples
8.72 ± 0.08 n/minute	48.7 ± 0.5	128 ± 1
Expected single bubbles in PICO-60 from Simulation		
5.3 ± 0.5 Background alphas.		
91 ± 9 Nuclear recoils.		
5.7 ± 0.6 (n,α) type reactions.		
0.63 ± 0.07 (n,^{x}H) type reactions.		

Table 5: Percentages of each reaction type from the simulated 40 cm placement of ^{252}Cf.

^{252}Cf – 60 ± 2.4 cm from bottom of source tube		
Reaction Type	Single Bubble (%)	Multiple Bubbles (%)
Nuclear Recoil	92.6 ± 0.8	97.4 ± 0.8
(n,α)	6.65 ± 0.07	2.53 ± 0.03
(n,^{x}H)	0.76 ± 0.02	0.105 ± 0.009
^{19}F(n,α)^{16}N	84.8 ± 0.9	46 ± 1
^{19}F(n,α+n)^{15}N	9.8 ± 0.3	52 ± 1
^{12}C(n,α)^{9}Be	5.3 ± 0.4	1.50 ± 0.05
^{13}C(n,α)^{10}Be	0.02 ± 0.07	0.02 ± 0.01
^{19}F(n,p)^{19}O	95 ± 3	95 ± 11
^{19}F(n,d)^{18}O	4 ± 1	2.2 ± 0.8
^{19}F(n,n+p)^{18}O	0.3 ± 0.1	1.9 ± 0.3
^{19}F(n,t)^{17}O	-	1.1 ± 0.3
PICO-60 Data – Run Type 15: Singles to Multiples 31 ± 3 %		
Live Time (min)	Singles	Multiples
5214 ± 8	205 ± 14	624 ± 25
Prediction from Simulation: Singles to Multiples 34.2 ± 0.4 %		
Neutron Yield	Singles	Multiples
8.72 ± 0.08 n/minute	114 ± 1	333 ± 3
Expected single bubbles in PICO-60 from Simulation		
11 ± 1 Background alphas.		
180 ± 13 Nuclear recoils.		
13 ± 1 (n,α) type reactions.		
1.5 ± 0.1 (n,^{x}H) type reactions.		

Table 6: Percentages of each reaction type from the simulated 60 cm placement of ^{252}Cf.

^{252}Cf – 80 ± 2.4 cm from bottom of source tube		
Reaction Type	Single Bubble (%)	Multiple Bubbles (%)
Nuclear Recoil	93.1 ± 0.9	97.5 ± 0.5
(n,α)	6.16 ± 0.07	2.36 ± 0.04
(n,^{x}H)	0.73 ± 0.02	0.10 ± 0.01
^{19}F(n,α)^{16}N	84 ± 1	46 ± 1
^{19}F(n,α+n)^{15}N	9.8 ± 0.4	53 ± 1
^{12}C(n,α)^{9}Be	6.1 ± 0.4	1.70 ± 0.06
^{13}C(n,α)^{10}Be	0.06 ± 0.08	-
^{19}F(n,p)^{19}O	93 ± 3	95 ± 13
^{19}F(n,d)^{18}O	7 ± 1	4 ± 1
^{19}F(n,n+p)^{18}O	0.2 ± 0.1	0.9 ± 0.4
^{19}F(n,t)^{17}O	0.2 ± 0.3	-
PICO-60 Data – Run Type 16: Singles to Multiples 31 ± 6%		
Live Time (min)	Singles	Multiples
1488 ± 2	45 ± 7	136 ± 12
Prediction from Simulation: Singles to Multiples 36.9 ± 0.5 %		
Neutron Yield	Singles	Multiples
8.72 ± 0.08 n/minute	31.2 ± 0.3	84.6 ± 0.8
Expected single bubbles in PICO-60 from Simulation		
3.0 ± 0.3 Background alphas.		
39 ± 7 Nuclear recoils.		
2.6 ± 0.4 (n,α) type reactions.		
0.31 ± 0.05 (n,^{x}H) type reactions.		

Table 7: Percentages of each reaction type from the simulated 80 cm placement of ^{252}Cf.

AmBe – 144 ± 2.4 cm from bottom of source tube		
Reaction Type	Single Bubble (%)	Multiple Bubbles (%)
Nuclear Recoil	90 ± 5	95 ± 4
(n,α)	8.7 ± 0.4	5.1 ± 0.3
(n,^{x}H)	1.3 ± 0.1	0.19 ± 0.07
^{19}F(n,α)^{16}N	80 ± 4	43 ± 4
^{19}F(n,α+n)^{15}N	14 ± 1	54 ± 4
^{12}C(n,α)^{9}Be	6 ± 2	2.4 ± 0.2
^{13}C(n,α)^{10}Be	-	-
^{19}F(n,p)^{19}O	93 ± 10	97 ± 51
^{19}F(n,d)^{18}O	7 ± 4	2 ± 4
^{19}F(n,n+p)^{18}O	-	2 ± 1
^{19}F(n,t)^{17}O	1 ± 1	-
PICO-60 Data – Run Type 2: Singles to Multiples 28 ± 5 %		
Live Time (min)	Singles	Multiples
1611 ± 5	49 ± 7	163 ± 13
Prediction from Simulation: Singles to Multiples 48 ± 1 %		
Neutron Yield	Singles	Multiples
67.3 ± 0.7 n/s	97 ± 2	204 ± 4
Expected single bubbles in PICO-60 from Simulation		
3.2 ± 0.3 Background alphas.		
41 ± 7 Nuclear recoils.		
4.0 ± 0.6 (n,α) type reactions.		
0.6 ± 0.1 (n,^{x}H) type reactions.		

Table 8: Percentages of each reaction type from the simulated 144 cm placement of AmBe.

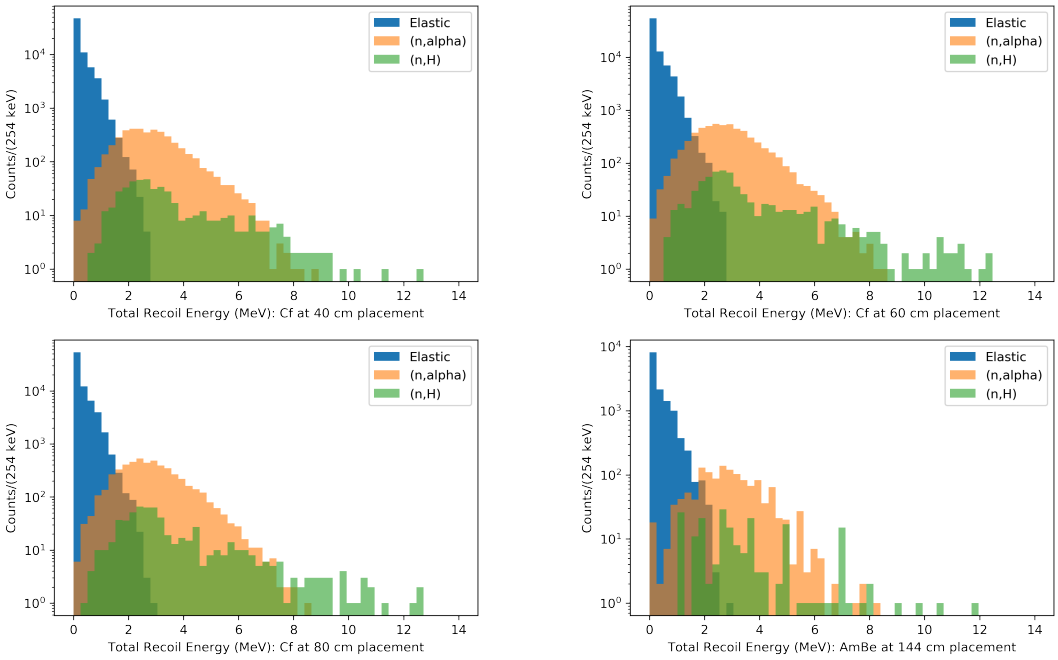

Figure 20: The total recoil energy deposited to every single bubble event from simulations. Blue, nuclear recoils from elastic scattering. Orange, (n,α) type reactions. Green, (n,^{x}H) type reactions.

The key ingredient that makes events distinguishable in AP is the amount of energy above threshold deposited to the region of a single bubble. The total recoil energy above threshold for every nucleus is added together to obtain the subplots of Figure 20. The blue distribution shows the total recoil energy deposited via nuclear recoils with ^{19}F or ^{12}C, and the orange/green curve shows the total recoil energy deposited to either (n,α) or (n,^{x}H) type reactions.

For example, if the ^{19}F(n,α)^{16}N reaction takes place the energy of the alpha and nitrogen nuclei are combined and binned appropriately. The reason for this addition will be made clear in the next section, but the key take away is the tail of these distributions. The background alphas are distinguishable in AP because their energies range from 5 - 8 MeV. In Figure 20, the total energy deposited from nuclear processes reaches energies up to 13 MeV. This means that fast neutrons can cover the entire AP region between nuclear recoils

and background alpha particles.

To study this, the results summarized in Figure 20 and Tables 5, 6, 7, and 8 are used to conduct a molecular dynamics simulation. This will provide a first order estimate for AP values from these reactions at all energies.

8 Molecular Dynamics Simulation

To predict the acoustic energy emitted during bubble expansion, the Large-Scale Atomic/ Molecular Massively Parallel Simulator (LAMMPS) [46] is run using the analysis framework developed by T. Kozynets, et al. [47].

LAMMPS offers the ability to model fluid dynamics, making it possible to follow bubble formation in C_3F_8 over time. Fitting the expanding radius of a bubble to the LAMMPS simulation, T. Kozynets et at. showed that the Acoustic Parameter (AP) for single bubble background alpha and nuclear recoil like events can be predicted. The outcome demonstrated clear differentiation in the two AP distributions, agreeing with measurements from the PICO-60 experiment.

Using this tool-set, the AP reconstruction can be extended to analyze the nuclear reactions discussed in Chapter 7. The result is fitted to calibration data from the PICO-60 detector and finally compared to the simulated prediction summarized in Tables 5, 6, 7, and 8.

8.1 The Simulation

To reproduce operating conditions of PICO-60, the 3D volume in LAMMPS is defined by a system of molecules interacting according to the Lennard-Jones (LJ) potential [48]. In this way, the fluid is modelled by two thermodynamic parameters: the characteristic energy (ε) and distance (σ). To reflect the active volume, ε and σ are adjusted to produce a target

that matches the critical temperature and density of C_3F_8: ε = 0.0318 eV and σ = 0.533 nm [47].

The simulation is initialized by assigning every molecule a thermal velocity that reflects a compressed state of the detector. Running LAMMPS, the thermal motion of the particles is tracked and the overall pressure of the fluid is maintained under NPT conditions; constant number of atoms (N), pressure (P), and temperature (T). Once the volume reaches equilibrium, the thermal velocity of every molecule is dropped to achieve a moderately super-heated state. Once equilibrium is again reached, the system now mimics the pressure drop applied by PICO; which brings the system to operating conditions resembling PICO bubble chambers operated at $\approx$14°C.

At this step, the simulation is ready to produce a bubble by introducing a sudden deposition of energy. This is modelled by applying a heat spike to the stable fluid, scaled to reflect the energy deposition from incoming radiation with energy density and travel length matching the type of particle interacting in the bubble chamber. The deposition is approximated by increasing the kinetic energy of the molecules inside a cylindrical volume, so that the energy of the process being modelled reflects the deposited energy. The length of the cylinder is adjusted to the penetration depth of the particle in C_3F_8, determined using the SRIM toolkit [49]. Once spiked, the simulation is left to evolve over time and a bubble is formed, if the amount and density of deposited energy is above threshold.

8.2 Extending the Acoustic Parameter (AP) Model

The primary difference between the reactions modeled in [47] and the ones currently being investigated (see Table 1), is the number of recoiling nuclei. Figure 21 sketches how a typical alpha or NR like reaction (left) deposits energy into the detector in comparison to neutron induced nuclear reaction events (right). The amount of energy being deposited

and the penetration depth of the incident particle separates the processes. Otherwise, they all describe charged single particles traveling through the same media. Background alpha particles deposit MeV scale energies over μm distances, while a single neutron scatter deposits keV scale energies over nm distances. The nuclear reaction shown deposits MeV scale energies into two regions that cover μm distances; similar to the background alpha scenario.

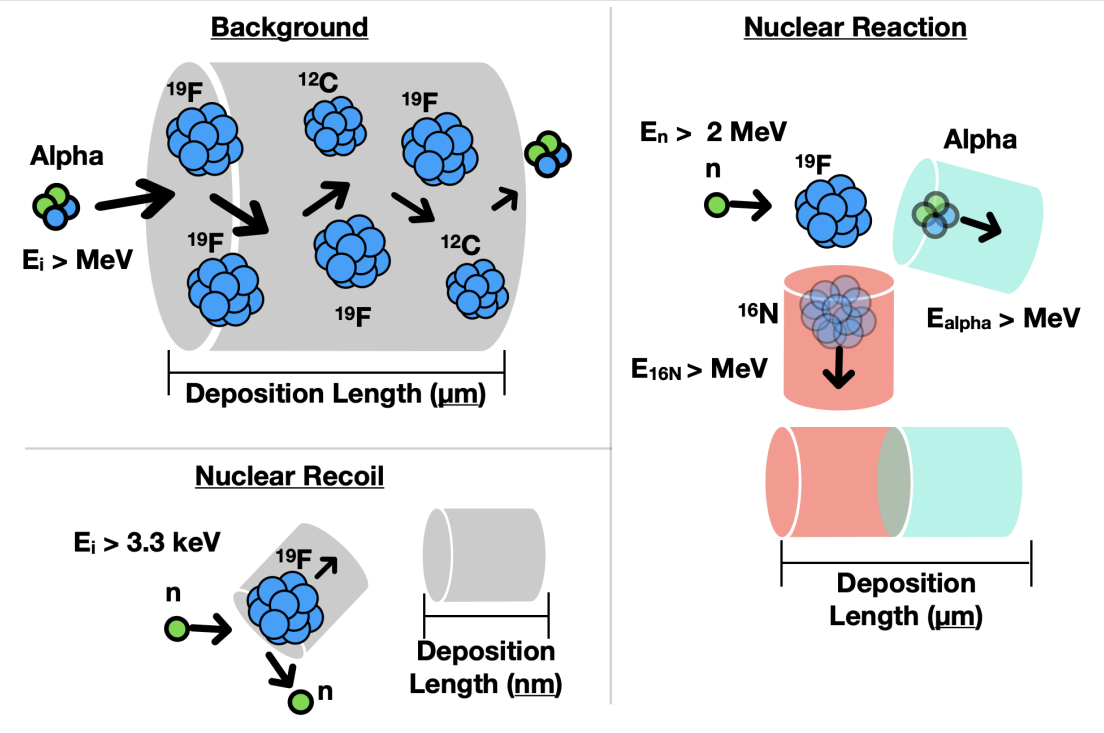

Figure 21: Symbolic example of events modelled by the molecular dynamics simulations. A neutron or alpha particle (left) enters the detector with energy above threshold, and deposits the energy into a region being characterized by a cylindrical volume. The length travelled before the particle energy falls below threshold is denoted the deposition length. The new case (right) models a fast neutron splitting the freon atom into a nitrogen and alpha particle. Each product will carry away kinetic energy that is deposited into the target fluid. To simplify the kinematics, the recoil energy and deposition length will be the net sum of every recoiling particle.

In the case of neutron reactions, for example ^{19}F(n,α)^{16}N, the products introduce additional particles, α and ^{16}N, with associated kinetic energies. These nuclei each deposit

enough energy to generate bubbles, which evolve and combine to a single macroscopic observation. Currently, merging bubbles are not modelled by the molecular dynamics simulation, which use linear extrapolation to scale the energies and deposition lengths for single particle events to reconstruct the acoustics, see next sub-section.

The contribution from joining bubbles to AP has not been studied. The current analysis addresses how well the single bubble extrapolation works for nuclear reactions. Simplifying the geometry to single bubble events is expected to be an incomplete description of the nuclear reactions being studied, because it's unclear how merging bubbles would affect bubble growth and in turn the AP. The single bubble model will provide a first order estimate on where these events show up in the log(AP) distribution.

Included in Figure 21 is an example of the energy deposited from a nuclear reaction. Here the neutron comes in and breaks the fluorine atom into an alpha particle plus nitrogen. Due to the resolution of the cameras, the two emitted particles will evolve to form a single bubble, even if they deposit their energies independently. For example, if the products deposit energy within 0.5 mm of the each other, they will appear as a single bubble by the time it expands to trigger the camera system.

To incorporate these energies while preserving the analysis framework of [47], the total energy and length of deposition will be introduced in the LAMMPS simulation as the sum of the individual particles. This provides a first order estimate to modeling the AP value for multi-particle energy depositions.

Simulating Bubble Expansion

From the PICO-60 simulations described earlier, the recoil energy of each charged particle is known for every (n,α) and (n,^{x}H) type reaction (see Figure 20). The remaining ingredient is the deposition length of each particle, which is calculated on an event by

event basis using data from the SRIM package [49].

SRIM works by first defining a target (C_3F_8) at a specific density (1,379 kgm^{-3}). To run, charged particles with energies between $0-10$ MeV are simulated into the volume and the toolkit returns the calculated deposition length. Figure 22 shows an example of the SRIM output; these curves are interpolated to calculate the deposition length from the particle's known energy. For example, if beryllium is produced in a neutron reaction with 3 MeV of kinetic energy, it will travel ≈ 10 μm in the C_3F_8.

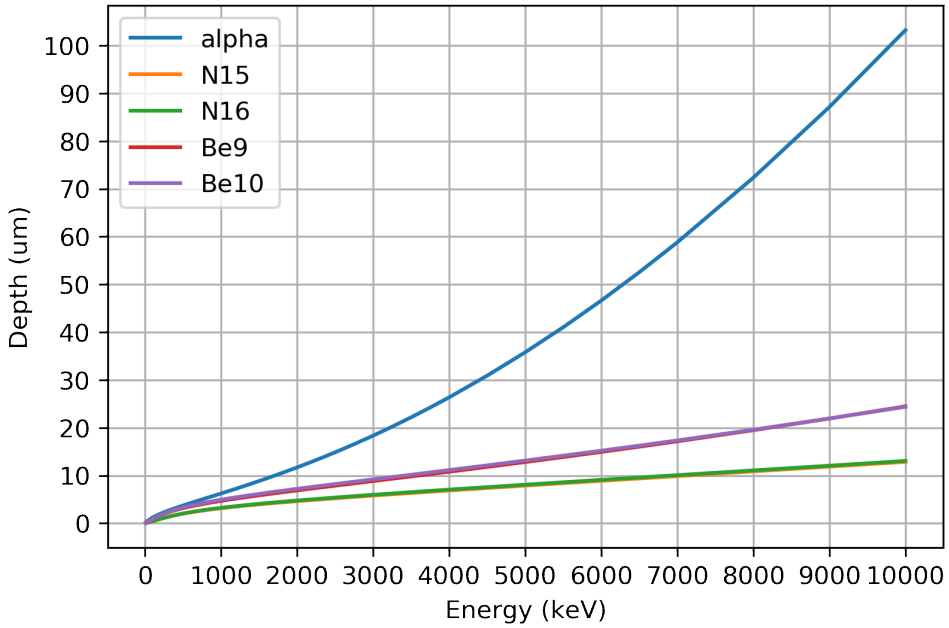

Figure 22: Example output from the SRIM package. Shown here is the penetration depth for a range of particles fired into a volume of C_3F_8 at various energies. For example, if $^{19}F(n,\alpha)^{16}N$ takes place the recoil energies of the α and nitrogen nuclei are used to interpolate the penetration depths, which are then added together for the total.

The reason recoil energy and penetration depth are required inputs to the model, is because they are directly used to calculate the initial conditions, R_s and t_s, used to solve the

differential equation for the bubble evolution in [47], referenced below:

$$\frac{dR}{dt} = -\left[\frac{A^2\sqrt{t-t_s}}{B} + \frac{2\nu_l}{R}\right] + \sqrt{A^2 - \frac{2\gamma}{\rho_l R} + \left(\frac{2\nu_l}{R} + \frac{A^2\sqrt{t-t_s}}{B}\right)^2} \tag{5}$$

Equation 5 is used to describe the bubbles radius, R, growth over time, t. t_s describes the time at which the bubble becomes spherical with radius R_s (initial conditions). ν_l is the kinematic viscosity, γ is the surface tension, ρ_l is the liquid density, and A/B are described by:

$$A = \sqrt{\frac{2h\rho_v\Delta T}{3\rho_l T_{sat}}}, \tag{6}$$

$$B = \sqrt{\frac{12}{\pi a_l}}\left(\frac{\Delta T c_l \rho_l}{h\rho_v}\right). \tag{7}$$

h is the enthalpy of vaporization, ρ_v is the vapor density, ΔT is the liquid superheat above the saturation temperature T_{sat}, a_l is the thermal diffusivity of the liquid, and c_l is the liquid heat capacity.

Following the simplifications outlined in [47], the equation is re-written as:

$$\frac{dR}{dt} = -\left[\frac{a\sqrt{t-t_s}}{B} + \frac{b}{R}\right] + \sqrt{a - \frac{c}{R} + \left(\frac{b}{R} + \frac{a\sqrt{t-t_s}}{B}\right)^2}. \tag{8}$$

Parameters a, b, c, and B are obtained by fitting the equation to the LAMMPS simulation as the bubble grows from the heat spike described earlier. This approach is used because it's undetermined how inter-molecular interactions contribute to the bubble growth; for example, if fluid properties like ν_l, γ, ρ_l, etc. are affected by the mode of energy deposition (merging bubbles or energy/length scales). Allowing the four parameters to float provides consistency across simulations. The fit results are:

$$a = A^2 = 313.29\frac{m^2}{s^2},$$

$$b = 2\nu_l = (36.6 \pm 0.8) \times 10^{-6} \frac{m^2}{s},$$

$$c = \frac{2\gamma}{\rho_l} = (5.3 \pm 0.1) \times 10^{-6} \frac{m^3}{s^2},$$

$$B = 0.0086 \pm 0.0002 \left(\frac{m}{s}\right)^{\frac{1}{2}}.$$

To solve the differential equation, the initial conditions when the bubble becomes spherical are calculated based on the linear extrapolation equations provided in [47]:

$$R_s\,[nm] \approx (0.38 \pm 0.03)\, l_{cyl}\,[nm] + (217 \pm 27)\, \frac{E_{dep}}{l_{cyl}} \left[\frac{keV}{nm}\right] \tag{9}$$

$$t_s\,[ns] \approx (0.082 \pm 0.006)\, l_{cyl}\,[nm] \tag{10}$$

The units in brackets describe the expected units of the input values E_{dep} and l_{cyl}. These two inputs are extracted from simulations and SRIM interpolation as described before.

For the multi-particle extension, the deposition length (l_{cyl}) and energy (E_{dep}) is calculated as the sum for all particles in the reaction. For example, a neutron reacting with ^{19}F can produce an alpha particle along with ^{16}N. Meaning:

$$E_{dep} = E_\alpha + E_{N_{16}}, \tag{11}$$

$$l_{cyl} = l_\alpha + l_{N_{16}}. \tag{12}$$

This allows the initial conditions shown in Equations 9 and 10 to be calculated and used to solve the ordinary differential equation shown in Equation 5. The result is a time dependent radius, which is directly related to the volume:

$$V(t) = \frac{4}{3}\pi R^3(t). \tag{13}$$

The evolution of Equation 13 over time contributes to the total acoustic power, P(t), radiated in all directions as sound waves by:

$$P(t) = \frac{\rho_l \ddot{V}^2}{4\pi c}. \tag{14}$$

The second order derivative of V is proportional to the acoustic amplitude in the fluid. Taking the fast Fourier transformation and integrating over the frequency range measured by the piezo sensors (1-300 kHz), the AP value is obtained [47].

Running these calculations for every event simulated using the AmBe and ^{252}Cf sources, the AP distribution for nuclear recoils, background alphas, (n,^{x}H) and (n,α) type reactions are obtained. The final results are shown in Figure 23.

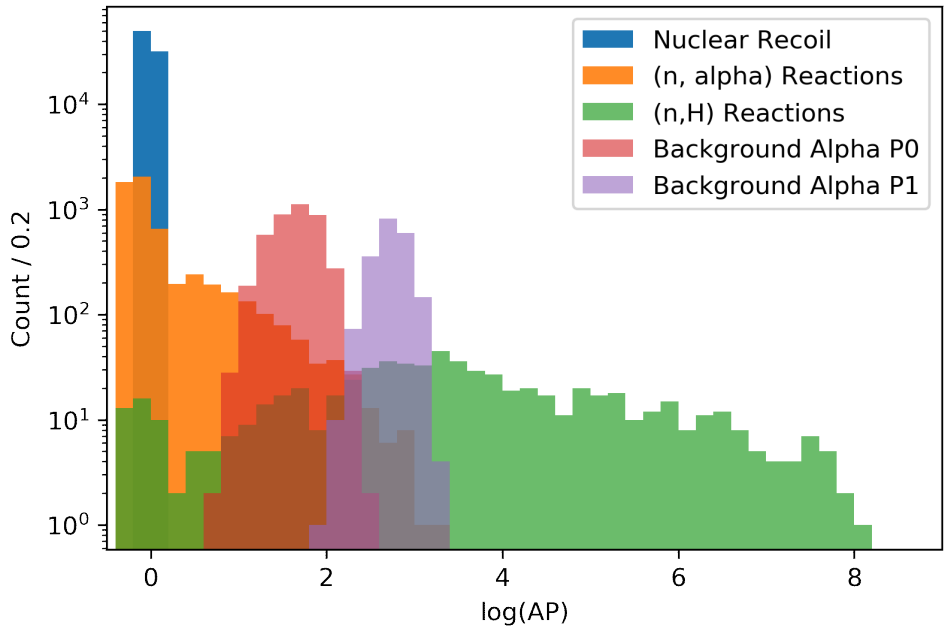

Figure 23: Summary of AP results from simulated sources. The nuclear recoil distribution, blue, is sharply peaked without any tail. Every distribution is scaled such that the NR events are centered around zero. The (n,α) type reactions, orange, are peaked at low AP with a continuous distribution extending out to a log(AP) $\approx$ 3. The (n,^{x}H) type reactions, green, are broadly spread out to log(AP) $\approx$ 8. The background alpha events from internal ^{222}Rn decays, red and purple, are clearly distinct from the NR peak.

The results are scaled such that the nuclear recoil peak, blue distribution, is centered around zero. The red and purple distributions show the expected alpha backgrounds, which agree with [24, 47] as their AP values sit to the right of the NR peak and are clearly distinguishable. The (n,α), orange, and (n,^{x}H), green, type reactions show a very interesting distribution. Both have clear peaks near the NR distribution, but they also include a broad tail that extends past the NR peak and includes the region outside the background alpha log(AP) distributions.

This illustrates that events outside the NR and background alpha peaks could very well be caused by fast neutrons.

8.3 Fitting to Data

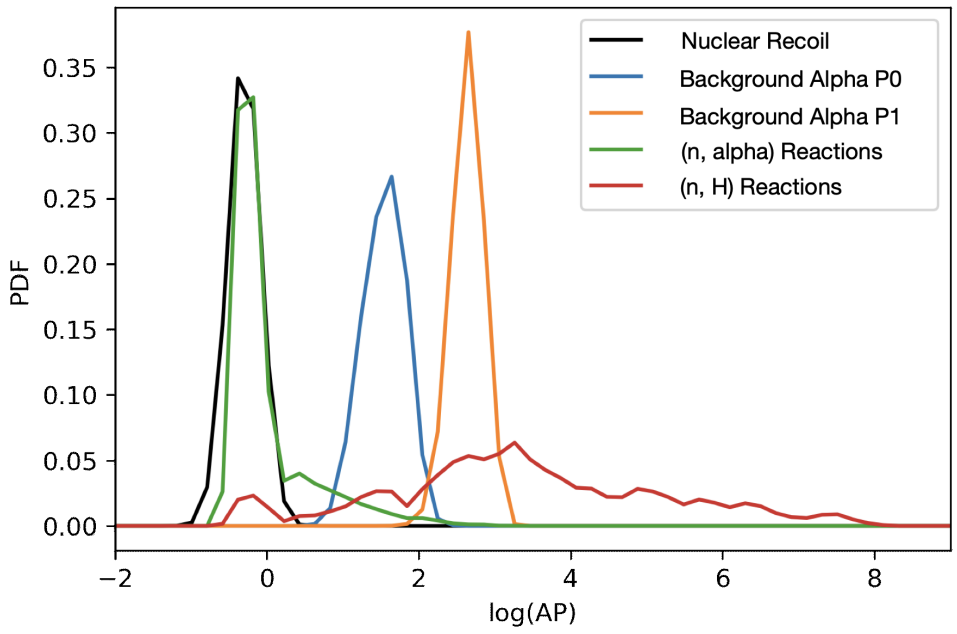

Figure 24: Example of the PDFs for the 60 cm ^{252}Cf run. Black is the nuclear recoil PDF, which has been smeared by 1σ [24]. Green and red are the (n,α) and (n,^{x}H) type reactions. Blue is the first peak (P0) of the alpha backgrounds, orange is the second peak (P1). All PDFs are normalized such that the area under the curve is equal to 1.

Converting the distributions in Figure 23 into a probability density function (PDF), the data from PICO-60 can be fitted to estimate how many of each reaction type is present and then compare this to the prediction presented in Tables 5, 6, 7, and 8.

Figure 24 shows the PDFs for each process. Black is the nuclear recoil PDF, which has been smeared by 1σ [24] to better represent the broad peak observed in the data. Green and red are the (n,α) and (n,^{x}H) type reactions. Blue is the first peak (P0) of the alpha backgrounds, containing the two energy depositions from the ^{222}Rn decay chain at 5.6 MeV and 6.1 MeV. Orange is the second peak (P1) for the background alphas, containing the 7.8 MeV peak.

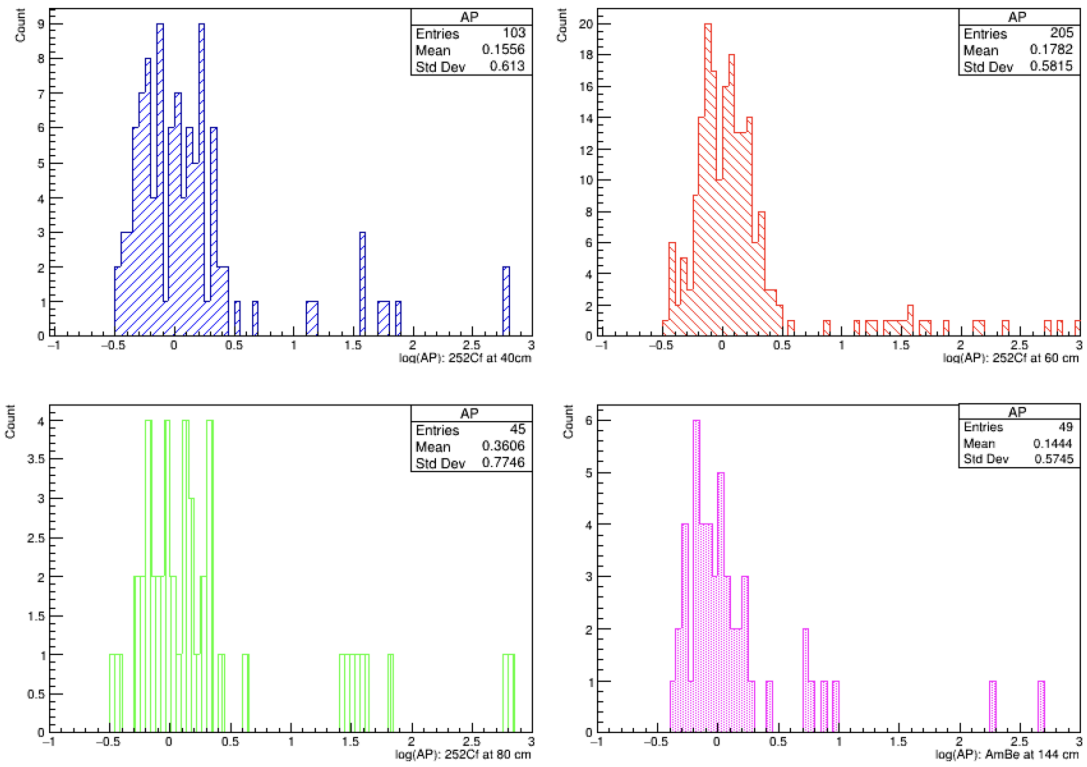

Figure 25: Single bubble data directly from the PICO-60 calibration runs, each operated at the same energy threshold and temperature. Distributions are shown after applying data quality, fiducial, and single bubble cuts. These histograms will be fit using the PDFs shown in Figure 24.

Figure 25 shows the raw single bubble data obtained from the four calibration runs running at the same threshold and temperature; Data quality and fiducial volume cuts have been applied, see Appendix A.

To fit the PDF's to these histograms, an equation of the form:

$$\Psi = A\alpha_0 + \frac{A}{2}\alpha_1 + B\eta + C\Omega + D\nu, \tag{15}$$

is used. Where α_0 and α_1 are the PDFs for the two alpha background peaks; η and Ω are the PDFs for (n,α) and (n,^{x}H) type reactions; ν is the PDF for the nuclear recoils. The remaining 4 parameters (A,B,C,D) are adjusted to minimize the residual, R, between Ψ and the PICO-60 data using a python minimization package[2]. The resulting parameters will indicate the number of each reaction type best matching the data. The final fit results are shown in Figure 26 and are compared to the prediction from simulation in Table 9.

The fit parameters summarized in Table 9 show a 1σ agreement with the simulated prediction for the ^{252}Cf source placed at 60 cm. This data set offers the best statistics, with a reduced χ^2 of 1.49. Despite low statistics, Gaussian uncertainties are used and it is recognized that Poisson errors would improve the χ^2. The result is consistent with the expectation that nuclear reactions will be present in the PICO-60 neutron calibration data. The AmBe source placed at 144 cm also agrees within 1σ, however the limited data set affected the fit convergence, with a reduced χ^2 of 2.16. The data for source placements at 40 and 80 cm have parameters that are 3σ from the simulated values, also affected by the limited data set.

The result concludes that the model provided by [47] offers a first order analysis tool for neutron reactions in PICO detectors. The 60 cm placement demonstrates that nuclear reactions can explain tail events in the log(AP) distributions, consistent with simulations.

[2]Python package: scipy.optimize.minimize

To improve this result, higher statistic calibration runs are required, as planned for PICO-40L (see last section.) The new detector will also offer improved acoustic resolution. The quality of acoustic data from PICO-60 limited the current data analysis, because several of the sensors failed which affected acoustic reconstruction.

The result also indicates that the simplifications in the model do not hinder agreement with simulations. To improve the accuracy of the AP values generated, a revised model could account for sound emission from merging bubbles.

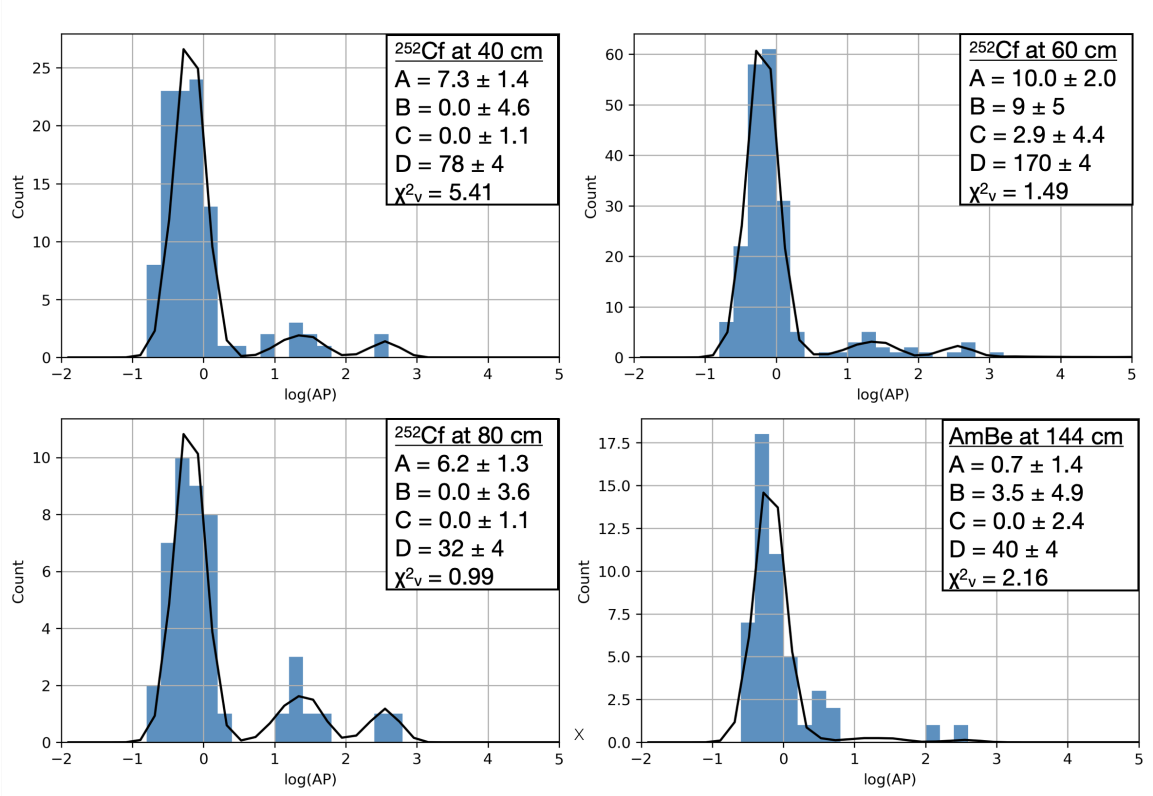

Figure 26: Resulting AP fits to PICO data. The optimized parameters (A,B,C,D) are shown for each source placement along with the reduced χ^2 value. Best fit results are the 60 and 80 cm placements. Limited statistics and/or data quality effect the fit convergence for 40 and 144 cm data sets.

40 cm ^{252}Cf Run		
Nuclear Recoil	78 ± 4	91 ± 9
Background alphas P0	7.3 ± 1.4	3.5 ± 0.3
Background alphas P1	3.7 ± 0.7	1.8 ± 0.2
(n,α)	0.0 ± 4.6	5.7 ± 0.6
(n,^{x}H)	0.0 ± 1.1	0.63 ± 0.07
60 cm ^{252}Cf Run		
Nuclear Recoil	170 ± 4	180 ± 13
Background alphas P0	10.0 ± 2.0	7.3 ± 0.7
Background alphas P1	5.0 ± 1.0	3.7 ± 0.3
(n,α)	9 ± 5	13 ± 1
(n,^{x}H)	2.9 ± 4.4	1.5 ± 0.1
80 cm ^{252}Cf Run		
Nuclear Recoil	32 ± 4	39 ± 7
Background alphas P0	6.2 ± 1.3	2.0 ± 0.2
Background alphas P1	3.1 ± 0.7	1.0 ± 0.1
(n,α)	0.0 ± 3.6	2.6 ± 0.4
(n,^{x}H)	0.0 ± 1.1	0.31 ± 0.05
144 cm AmBe Run		
Nuclear Recoil	40 ± 4	41 ± 7
Background alphas P0	0.7 ± 1.4	2.1 ± 0.2
Background alphas P1	0.4 ± 0.7	1.1 ± 0.1
(n,α)	3.5 ± 4.9	4.0 ± 0.6
(n,^{x}H)	0.0 ± 2.4	0.6 ± 0.1

Table 9: Comparing fit results (middle) to simulated prediction (right).

9 Analysis of Multi-Bubble Events

The processing of PICO images follows the framework developed by P. Mitra [50] for single bubble events. To perform the 3D reconstruction of single bubbles in the detector volume, at least two cameras are required. The images are first analyzed by a pixel search, which identifies the curved surface of bubbles in each camera and their 2D pixel coordinates. These coordinates are compared to a look-up-table, which projects the individual 2D camera pixels into the 3D volume. Using camera pairs, there are two lines projected into the detector and the location of closest approach is the 3D coordinates of the bubble.

This method offers sub-millimeter resolution on the bubbles physical location, but was never used for multi-bubble reconstruction, because in the dark matter search multi-bubble events are attributed to neutron backgrounds and therefore removed. One motivating question in a multi-bubble analysis is if the direction of the source can be recovered. Such information would help identify backgrounds that can also generate single bubbles in the detector. If identified, such sources could be removed in future detectors.

The exact order of bubble formation can never be reconstructed, because all bubbles appear simultaneously and don't offer any hints of which came first. However, the real problem is the random nature of the scattering particle. When a neutron enters the detector and undergoes 10+ collisions, it does so in a nearly random walk. The end result offers no clear trajectory that points from the first bubble to the last bubble.

To address if the reconstructed bubble positions provide additional information about the event, what can be done is an overall direction approach. This means the starting and end points are completely irrelevant, but the overall distribution of bubbles is used to attempt direction reconstruction. The algorithm presented in this section answers how well the direction of a line, minimized to pass through all the bubbles in an event about the center of gravity, ends up pointing to the source that caused it.

9.1 Mix-Match Reconstruction

To generate a data set of 3D reconstructed multi-bubble events, a new technique was required to reliably assign coordinates to each bubble. Single bubble reconstruction doesn't suffer from any ambiguity assigning a bubble's image to a location, because there's no concern that 2 unique bubbles might get mixed up when looking from different camera angles. Even doing an eye scan of multi-bubble events can prove frustrating, when trying to match one bubble to another.

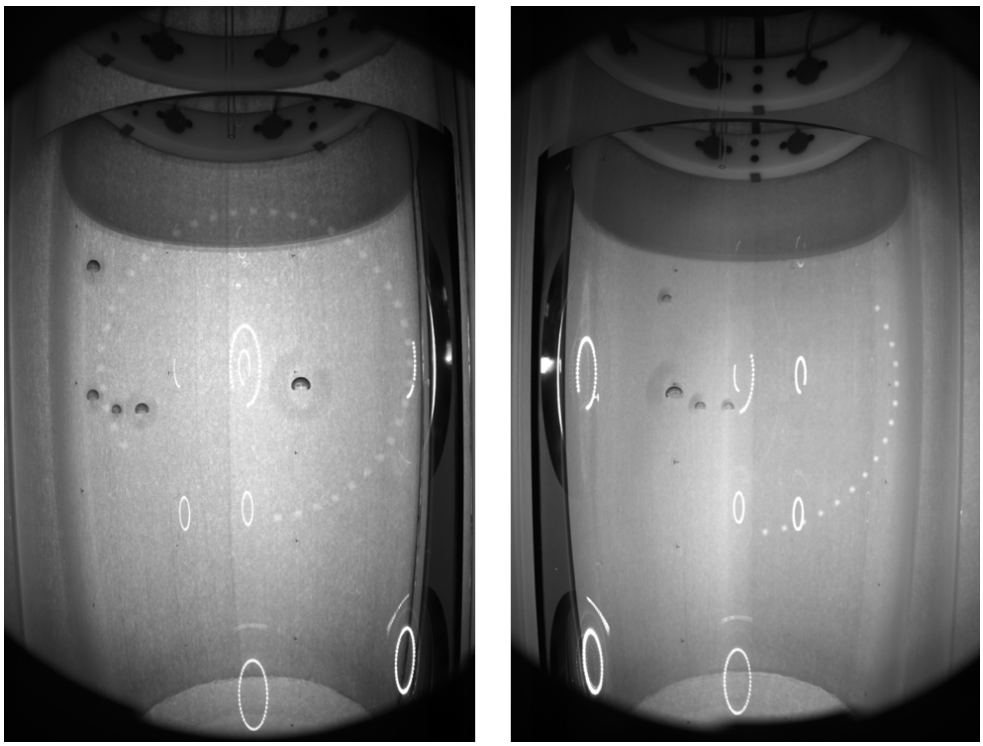

Figure 27: An example of a multi-bubble event as seen by two different cameras. The event includes 5 bubbles. Two of the bubbles appear to overlap in the image on the right, however they are clearly distinguishable in an earlier frame. The problem is making sure the correct set of pixel coordinates are paired for the reconstruction of all 5 bubble positions.

The problem becomes clear looking at Figure 27. This shows the same event, as seen by two different cameras. There are 5 bubbles present in both frames, however with the

change in angle two bubbles overlap in the image on the right. In an earlier frame the two bubbles are clearly distinguishable, however it takes some concentration to match the bubbles across cameras by eye. To allow a meaningful analysis, the correct assignment needs to be handled autonomously in order to reconstruct hundreds of events.

With that in mind, there is a saving grace in this problem. The sub-millimeter resolution offered by the single bubble reconstruction technique introduces an implicit tool. By matching every bubble as seen by one camera to every bubble seen by another, a list of (X, Y, Z) coordinates is generated. From this list, only one set of bubble positions will agree with the physical locations in the detector, the others will deviate substantially from the true bubble coordinates.

Repeating the calculation using a different camera combination, for the same event, a second list is generated; again with only one true set of coordinates. Cross referencing these two lists, there will be a unique (X, Y, Z) position for each bubble that matches within a millimeter. The false matches will disagree between 5-100 mm, making it easy to identify the correct positions. Therefore, the "mix-match" technique makes it possible to correctly obtain 3D coordinates for multi-bubble events. This is illustrated in Figure 28.

The limitation of this technique is that the bubble needs to be identified in at least three of the cameras. Bubbles missed by the pixel search or located outside the field of view of the cameras, cannot be reconstructed. For example, in Figure 28 from the pixel search camera 3 can only identify 3 of the 5 bubbles. One of the missed bubbles can be identified (by eye) in the field of view of the camera, however the pixel search didn't find it because the image is to dark where the bubble is located. The second missed bubble is outside the field of view of the camera and cannot be assigned pixel coordinates. This means the outcome of this analysis will reconstruct three of the bubbles, without further processing.

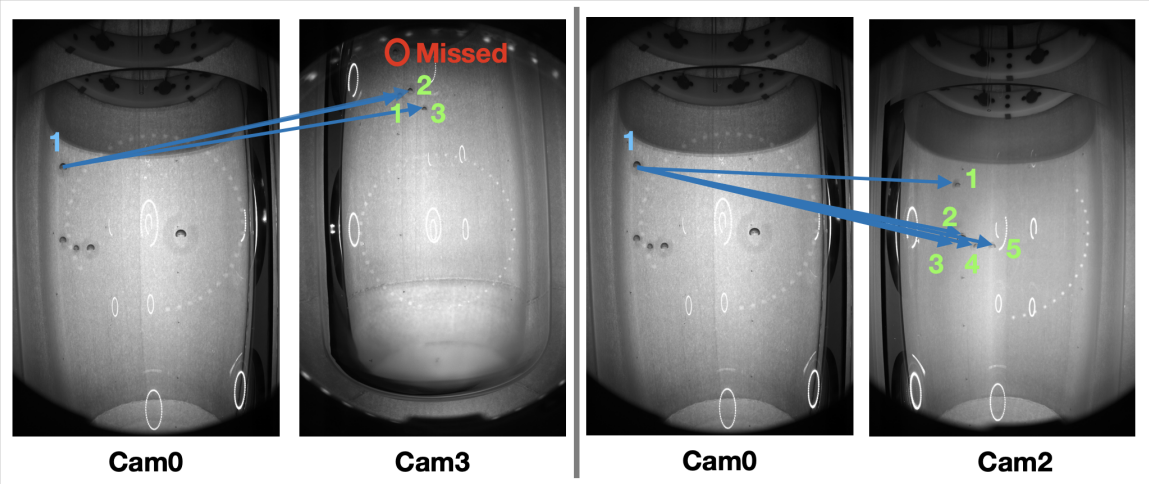

Figure 28: Mix-Match example. Bubbles in camera 0 are matched to every bubble in camera 3, generating a list of fifteen 3D coordinates. Bubbles in camera 0 are then matched to camera 2, generating a second list of twenty five 3D coordinates. Cross referencing these two lists, each bubbles correct set of coordinates will appear twice. The limitation, this technique requires at least three cameras to see the bubble.

From the 60 cm placement of the ^{252}Cf source, 101 multi-bubble events (with multiplicity >= 2) are reconstructed using the Mix-Match technique alone, with an uncertainty estimated at 1 bubble (see Figure 29).

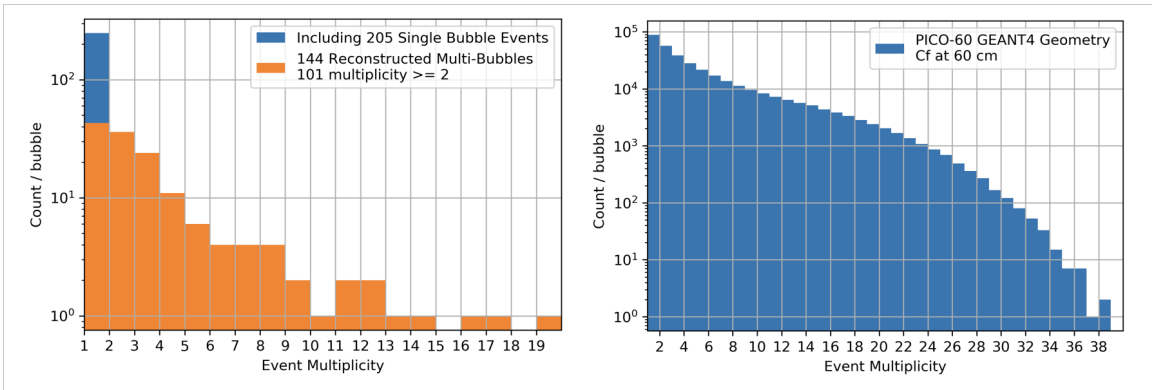

Figure 29: 3D reconstruction results (left) using the ^{252}Cf calibration data, placement at 60 cm. The Figure shows the bubble multiplicity for events reconstructed using the mix-match technique alone (orange). The uncertainty in number of bubbles reconstructed for each event is 1. The blue distribution includes the 205 single bubble events from that calibration run. Included in the right image is the bubble-multiplicity from GEANT4 simulation.

Also included in Figure 29 (left graph) is the additional 205 single bubble events from the ^{252}Cf calibration data at 60 cm (see Table 6). This is included to compare the reconstructed distribution to the GEANT4 simulation provided in the right graph. To unfold the neutron energy spectrum from these reconstructed multi-bubble events, the orange distribution from Figure 29 is first converted into a PDF (see Figure 30).

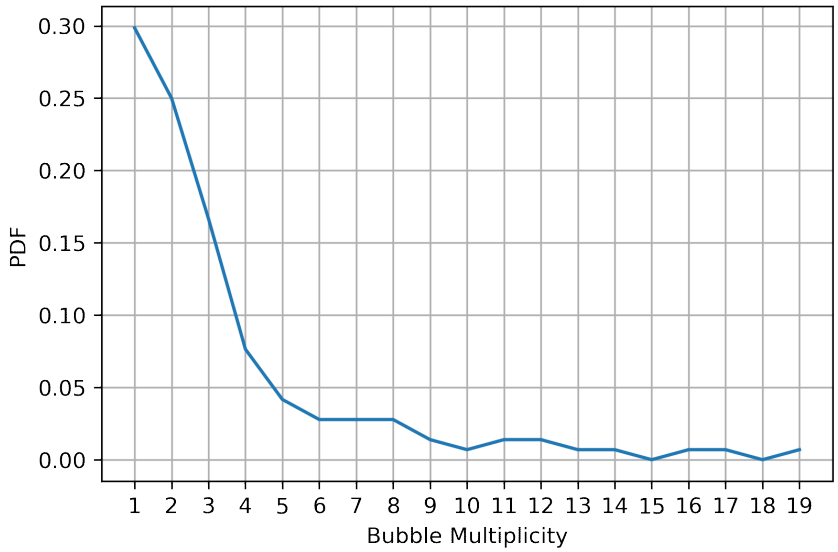

Figure 30: The probability density function for 3D reconstructed multi-bubble events from the PICO-60 calibration data.

From the GEANT4 simulations presented in Chapter 7, the energy of the neutron as it enters the detector can create a 2D spectrum of bubbles between 0 and 40 in the PICO-60 geometry (see Figure 31). Using the PDF in Figure 30, the energy spectrum of the neutrons entering the detector can be predicted.

The unfolding technique works by normalizing each multiplicity slice in Figure 31 by the number of events present in that horizontal distribution. Scaling these normalized slices by the probability of observing each multiplicity (see Figure 30), the neutron energy distribution is calculated by multiplying with the number of events reconstructed (101).

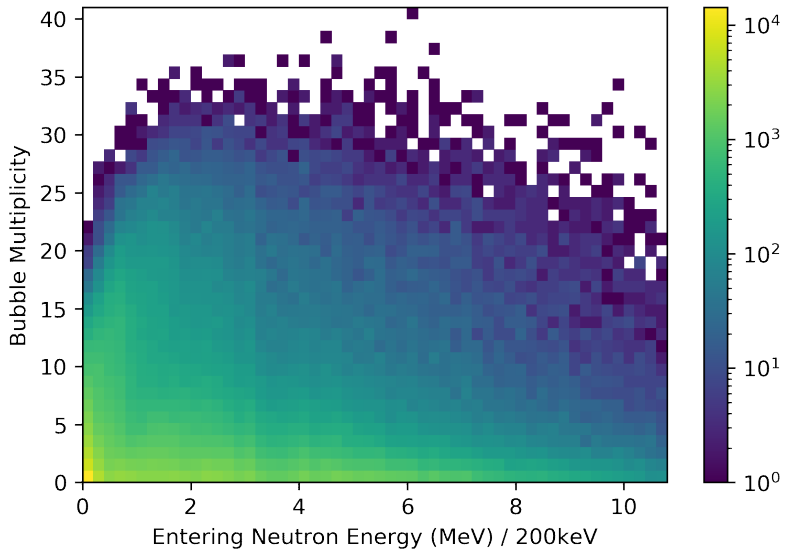

Figure 31: Bubble multiplicity as a function of neutron energy from the GEANT4 simulation using the PICO-60 geometry and 60 cm ^{252}Cf placement. Here, the effect of the neutron induced nuclear reactions is absorbed when compared to Figure 11, where all the neutron interactions were contained in the simulated volume.

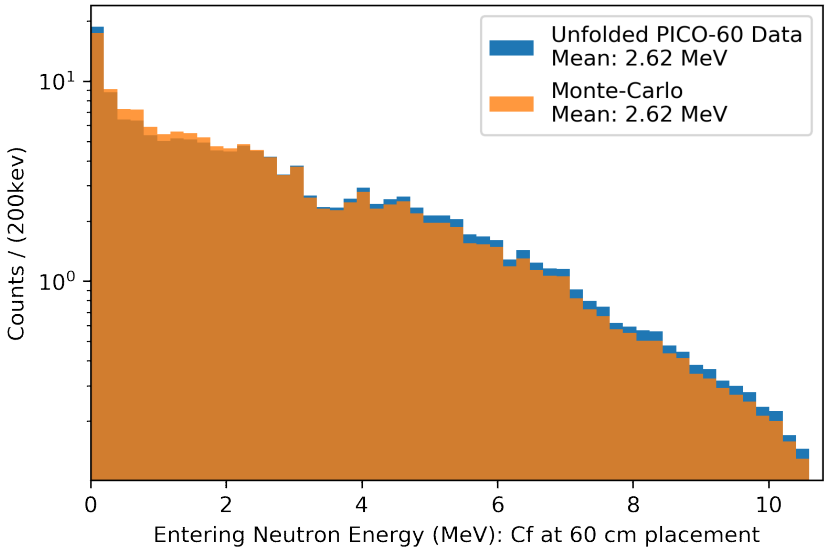

Figure 32: The unfolded neutron energy spectrum. This offers the first look at the energy of neutrons entering the detector to produce multi-bubble events. Overlaid is the energy spectrum from simulation, normalized to the number of bubbles reconstructed from data.

The result is shown in Figure 32, with the normalized Monte-Carlo result overlaid. This provides the first attempt to reconstruct the neutron energy spectrum for multi-bubble events measured by PICO-60. The unfolded spectrum suggests that slightly more high energy neutrons enter the detector than predicted by the Monte-Carlo.

The mix-match reconstruction method provides the first look at 3D reconstructed multi-bubble events measured by PICO-60. The coordinates are fully contained in the detector volume and the technique correctly assigns coordinates to bubbles visible in at least three cameras. The events reconstructed can be used to predict the neutron energy spectrum being measured, as demonstrated.

For the direction analysis discussed next, only events with at least 2 successfully reconstructed bubbles will be considered.

9.2 Line Fitting Neutron Direction

The goal when fitting a line to multi-bubble events is to reconstruct the location of the neutron source. To attempt the reconstruction of the neutron direction, a line through the center of gravity (see Equation 4) will be used to approximate the neutrons forward direction. This line will then be compared to the known source position from simulation and calibration runs. The attempt is considered a success, if the fitted line points to the source. The deviation of this line from the known source location will provide an upper estimate. The only input to the fit are 3D reconstructed bubble positions.

For the method attempted, the algorithm first determines the center of gravity (CoG) of a bubble cluster. The bubble positions are then fit to a line through the CoG, by adjusting the polar (θ) and azimuthal (ϕ) angles. The angles are changed to minimize the total distance of every bubble to the line. To visualize the steps involved, a 9 ± 1 bubble event from the PICO-60 calibration data (^{252}Cf at 60 cm: run 20170117_4 event 42) is shown in Figure

33. The 9 ± 1 bubbles are shown as blue dots. The green dot is the center of gravity. The orange dot is the neutron source located 60 cm from the bottom of the source tube. The dimensions of the active volume are represented by the red surface.

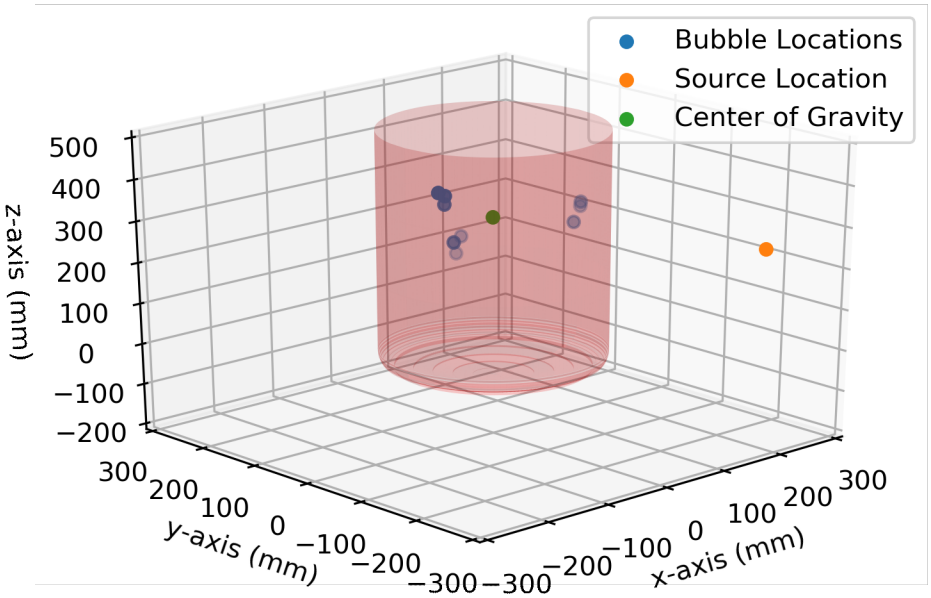

Figure 33: 9 ± 1 bubble event reconstructed from a PICO-60 calibration run. The blue dots represent the bubble coordinates within the active volume (red surface), the orange dot is the neutron source located 60 cm from the bottom of the source tube, and the green dot is the center of gravity of the bubble cluster.

The line fitting routine ultimately solves for two parameters, (θ, ϕ), to draw a through the CoG. Initially the angles are randomly generated. Then, the point of closest approach for each bubble to this random line is calculated and the distances between points are added. The python minimization routine then adjusts the values of θ and ϕ to return parameters where the total distance between the line and each bubble is at a minimum.

To run over thousands of events, the initial guess of (θ, ϕ) is first adjusted from the

random draw to improve the time required for convergence. This is demonstrated in Figure 34. The initial random angles are offset to obtain 6 evenly spaced lines that point in different directions. The total distance of every bubble to each line is calculated and the smallest returned value determines the next guess of θ and ϕ.

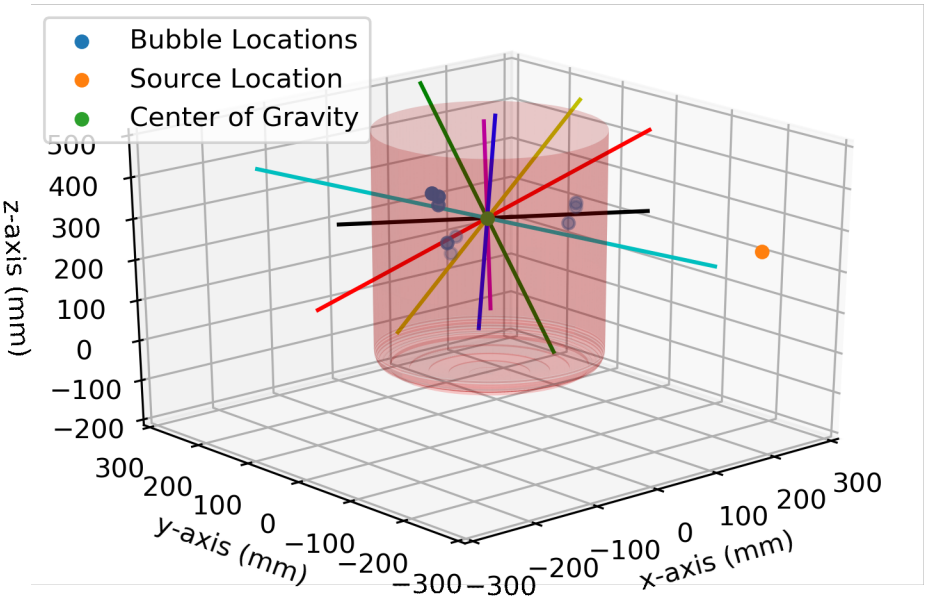

Figure 34: The algorithm's starting direction uses a line centered at the green dot and points in a random direction. To improve the convergence time of the minimizer, the random angles are adjusted to produce 6 evenly spaced lines that point in different directions. From these, the line in closest agreement to the bubbles will be used to begin the minimization.

The final output from the minimizer are values of θ and ϕ that draw a line through the cluster of bubbles. To determine the direction of agreement of this line to the source position, a second line is drawn from the center of gravity point (green) to the source location (orange), see Figure 35. The opening angle, η, between the minimized line (green) and the line connecting the center of gravity to the sources position (blue) is calculated. If the line

is pointing towards the source, η should be much less than 90°.

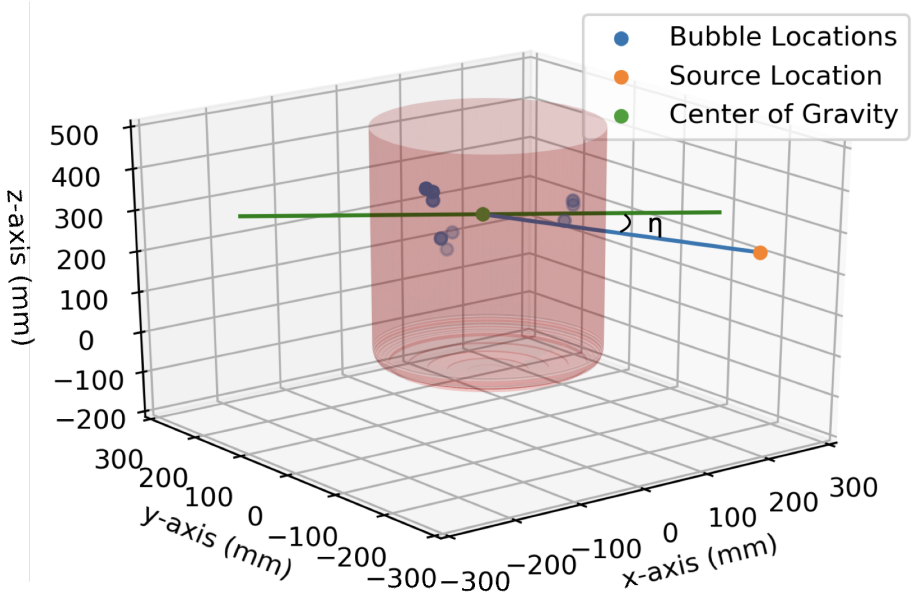

Figure 35: Final result from line fit. The green line is draw such that the distance of every bubble to the line is minimized. To compare across events, a blue line is drawn from the center of gravity (green) to the sources location (orange). The angle, η, between the blue and green lines determines how well the final fit points towards (or away) from the source. For this event $\eta = 14 \pm 3°$.

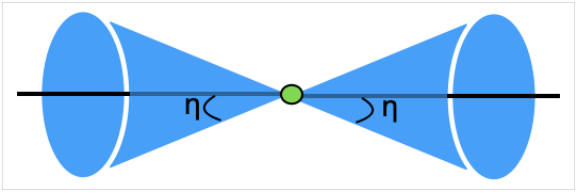

Figure 36: The direction of the line along with the opening angle narrows down the region of the source to be within the conic sections. The ideal scenario are small values of η in order to minimize the blue region. All directions outside the blue cones would be excluded as the source direction.

For the example shown, $\eta = 14 \pm 3°$, which narrows down two regions for the source as demonstrated by the blue cones in Figure 36. To be useful for an unknown background, η on average must be small in order to exclude directions outside the blue cones. The event in Figure 35 offers the ideal scenario, because the line does an okay job at narrowing down the source direction. This is not always the case, as demonstrated by the 4 ± 1 bubble event in Figure 37, where $\eta = 39 \pm 1°$.

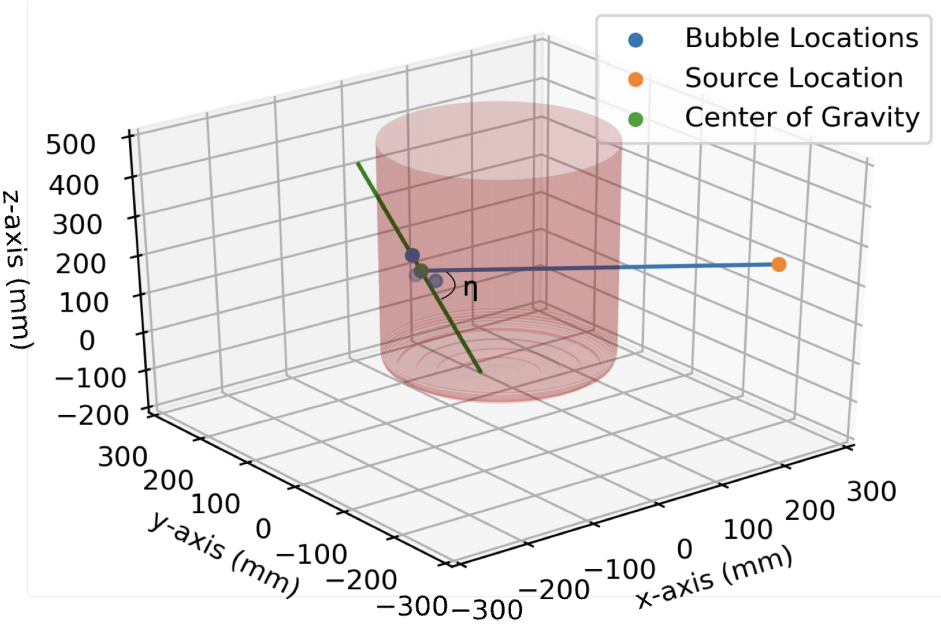

Figure 37: Second example of opening angle calculation using a 4 ± 1 bubble event: run 20161114_2 event 35. Here, $\eta = 39 \pm 1°$.

9.3 Opening Angle Analysis

To understand the meaning of the opening angles determined with the method described so far, opening angle distributions are calculated for three different simulations. The first uses multi-bubble events generated by GEANT4 in the large tank of C_3F_8 from Chapter 6, to determine the shape of the distribution for events with minimal leakage due to its size.

This is compared to the η distribution calculated for events simulated in GEANT4 using the PICO-60 geometry from Chapter 7. The expectation is that the second simulation will have a larger spread in angles, because the neutron is expected to leave the detector. The third simulation performs a toy Monte-Carlo that places bubbles randomly in the PICO-60 volume, to provide a random data set to compare results with. The final distribution shown is from the PICO-60 data that was reconstructed from the Mix-Match method (Section 9.1).

The distribution of η calculated for every multi-bubble event using the tank geometry in GEANT4, is presented in Figure 38. The values of η peak at 18° with a standard deviation of 24°.

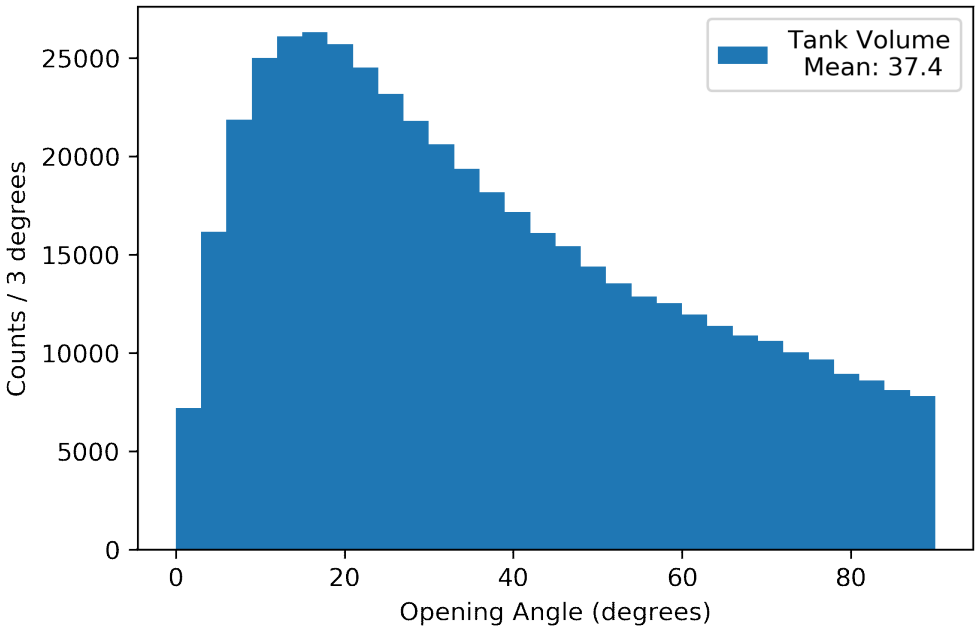

Figure 38: Opening angle results for GEANT4 simulated large tank geometry. The values of η peak at 18°, with a wide spread to larger angles.

The events used in the tank geometry are primarily contained within the tank due to the size. Using the PICO-60 geometry in GEANT4, it is expected that there will be an enhancement of large angles because the angle between the source and the detector is ap-

proximately orthogonal. Figure 39 shows that the opening angle distribution peaks at 90° with a wide spread to low angles. This is in contrast to the results obtained from the tank, indicating that the direction of the line cannot be used to narrow down the source location using this technique.

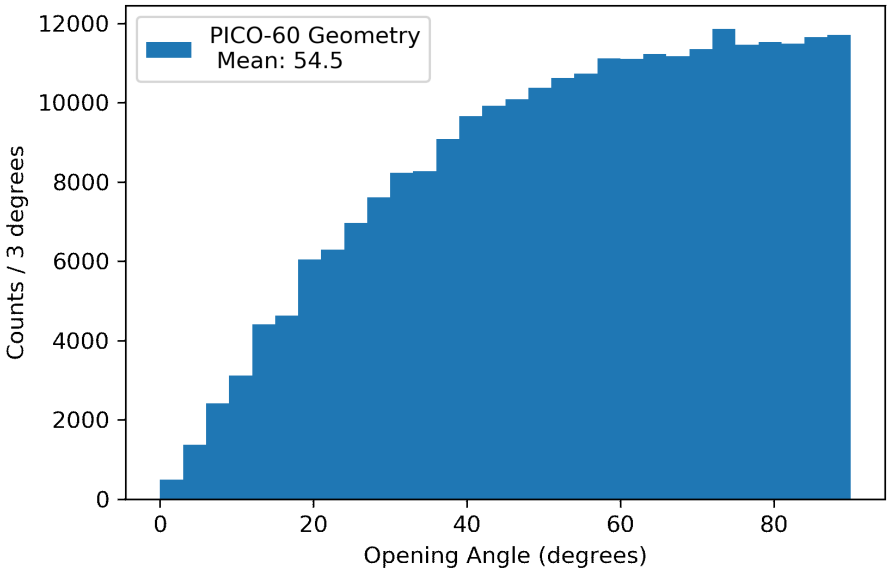

Figure 39: Opening angle results for multi-bubble events simulated in GEANT4 using the PICO-60 geometry. The broad distribution is not in agreement with the tank geometry.

To address if the events in the PICO-60 simulation mimic a random direction, the quartz jar geometry is isolated and random bubbles are simulated in it. This is done by first generating a bubble multiplicity from the PDF in Figure 30, then throwing the x, y, and z coordinates randomly into a region slightly larger than the C_3F_8 volume. If the bubble is within the target, it is kept and recorded as a bubble for the event. Generating 10,000 of these random events and running the minimization routine, Figure 40 is obtained.

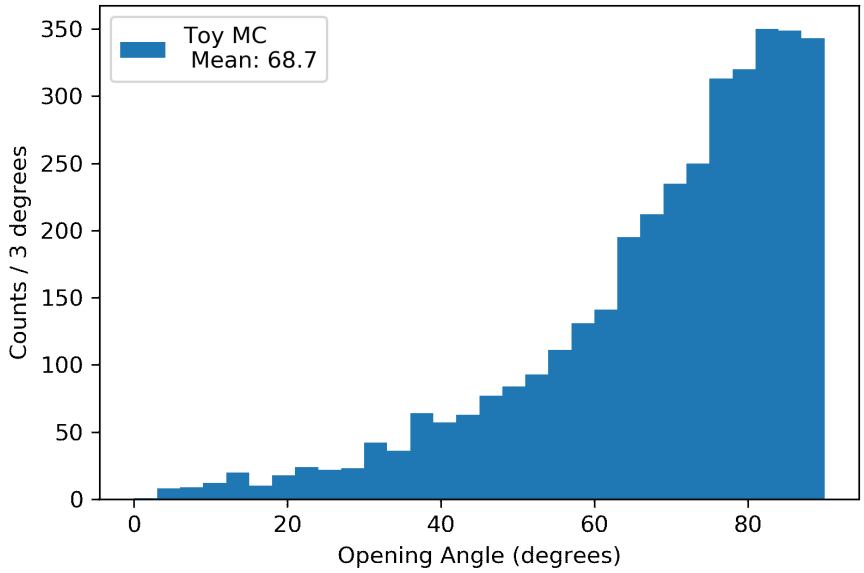

Figure 40: Toy Monte-Carlo simulating events in the PICO-60 volume, with a bubble multiplicity following the multi-bubble distribution reconstructed from PICO data (see Figure 30). Peak value at 81°. These random events do not agree with results simulated with the tank geometry (see Figure 38). The observation of large opening angles is in agreement with the GEANT4 PICO-60 geometry, however the distribution in Figure 39 is much broader, indicating the neutron events are not entirely random.

The events in the toy Monte-Carlo are similar to the PICO-60 geometry as they point away from the source, however the PICO-60 geometry does not appear completely random as the distributions are very different. The direction reconstruction is not pointing to the source location (within 20°) for events not fully contained, but is also not in agreement with a random direction.

The experimental data is shown in Figure 41. The peak value is in agreement with a random direction at 85°, however this cannot be concluded as completely random with the current statistics. With a larger data set the distribution could reflect Figure 39, where a modified fitting routine could be developed to resolve the non-random features.

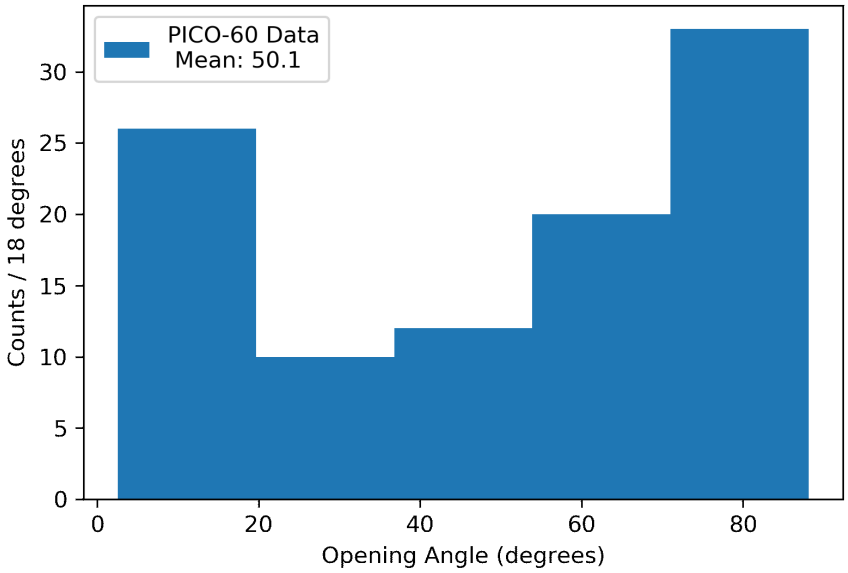

Figure 41: Opening angle calculated for PICO-60 multi-bubble events that are reconstructed in Figure 29. The peak value is at 85°, suggesting the data reflects GEANT4 simulations. Result is inconclusive without improved statistics.

The CoG minimization technique demonstrated that events primarily contained within the assigned geometry offer the best resolution at reconstructing source direction. This breaks down when using the small PICO-60 geometry, which showed a broad spread in opening angles that point away from the source direction. The upshot here is that the distribution does not fully reflect a random direction, an observation that could be further questioned with larger data samples.

Improved analysis could also address the difference in geometry between the simulated PICO-60 volume and the data reconstructed via the mix-match technique. The mix-match algorithm requires that at least three cameras can see the bubbles, which means the events reconstructed are all located in the middle of the detector. To pursue this attempt further, the simulations should be modified to be limited to events that can be detected by all camera positions.

10 PICO-40L Commissioning

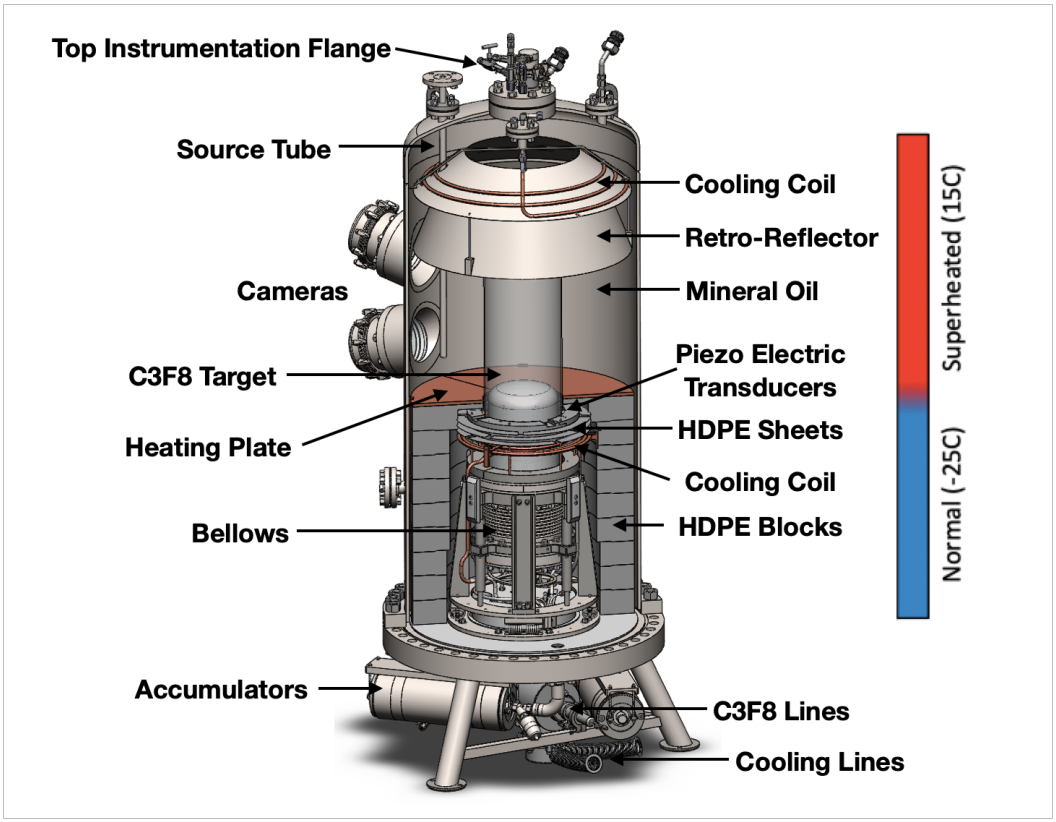

Figure 42: Schematic rendering of the PICO-40L detector designed to operate at SNOLAB. The right-side-up orientation uses two concentric quartz jars connected by a bellows. The design includes two thermally isolated regions. The warm region surrounds the C_3F_8 target and the cold region surrounds the stainless steel components. Data is collected by four offset cameras and piezo electric transducers coupled to the jars.

The PICO-40L detector is being commissioned at SNOLAB in the same water tank used before by PICO-60. The right-side-up design eliminates the water buffer found with the PICO-60 detector and improvements to the thermal, pressure, and acoustic systems were made compared to PICO-60 [51]. A schematic representation of the detector is shown in Figure 42.

The active liquid is contained between two concentric glass jars, removing the water

buffer used for PICO-60. Changing the pressure to the surrounding mineral oil, the bellows contracts/expands along guide rods which in turn sets the pressure of the target (C_3F_8). The volume within the pressure vessel is separated into two thermal regions. The warm region surrounds the jars to achieve a moderately superheated state, as described in Chapter 5. The cold region surrounds the stainless steel components of the bellows, which acts to prevent bubble formation in the C_3F_8 in contacts with the steel flanges.

The cold temperature is maintained using two cooling coils (see Figure 43), the inner coil sits inside the smaller jar and the external cooling coil sits outside the larger jar. The temperature in the warm region is controlled using resistive wires located under two copper heating plates. The larger plate is visible in Figure 42 and the smaller plate is visible in Figure 43.

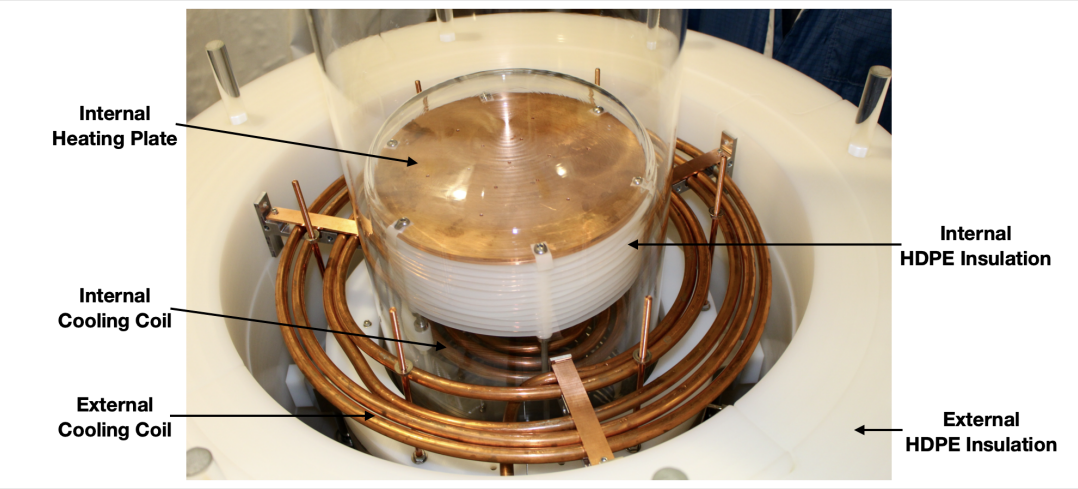

Figure 43: The cold region is cooled using two copper coils; the internal coil is visible within the smaller quartz jar, and the external coil sits outside the larger quartz jar. The warm and cold regions are insulated by HDPE. The internal region uses HDPE sheets to separate the copper heating plate from the internal coil. The external region is separated by HDPE blocks, not fully assembled in this image.

The two regions are insulated using high density polyethylene (HDPE). The internal region uses HDPE sheets that are located between the coil and plate. The external region

is surrounded by HDPE blocks and HDPE sheets on the Piezo ring (See Figure 42) to prevent convection in the oil. The warm region also includes a cooling coil located above the retro-reflector cones, used to remove excess heat.

The base flange of the detector, flipped upside-down, in detail is shown in Figure 44. The instrumentation flange houses Noshok and Setra pressure transducers (PT) that measure the pressure of the mineral oil; identical sensors are located in the top instrumentation flange (see Figure 42). The base instrumentation flange also includes two Gefran magnetic position sensors. These are measuring the bellows position using magnets connected to the movable bellows flange and the base position. Finally there is a Dytran sensor, used to measure fast pressure changes.

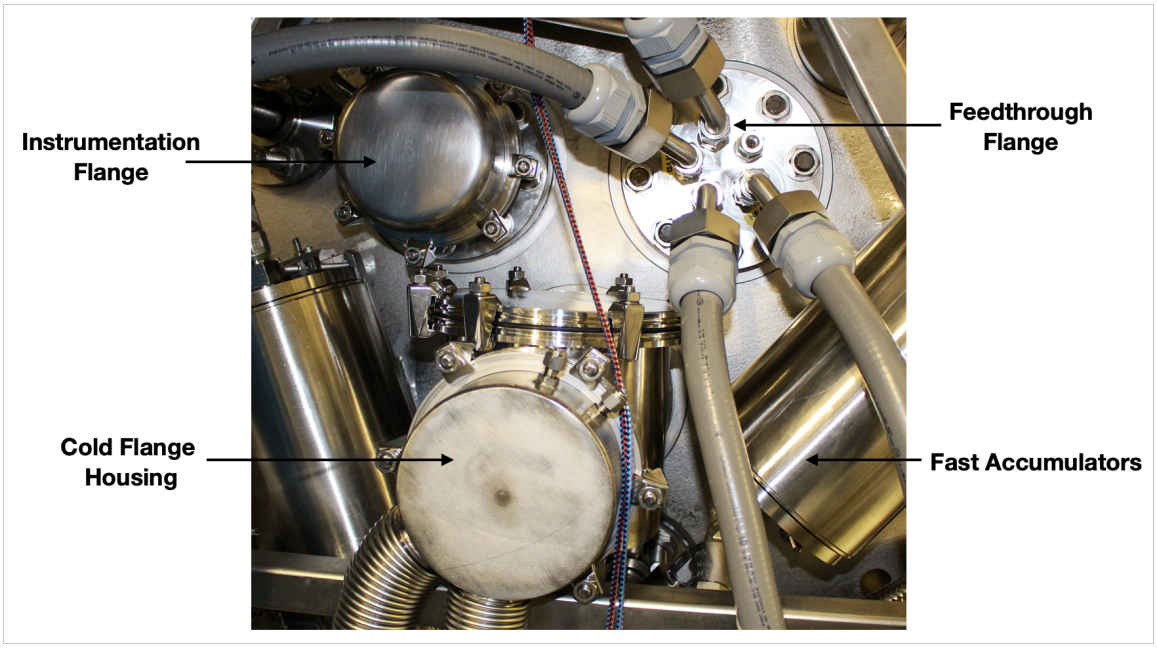

Figure 44: Underside of the PICO-40L base flange. The instrumentation flange houses pressure and positioning sensors that monitor operating conditions of the mineral oil and bellows positioning. The feedthrough flange manages electrical connections and mineral oil drainage. The cold flange houses the cooling coil feed-through connections and C_3F_8 fill/drain lines. Also mounted are 3 fast accumulators, which control the pressure of the mineral oil.

The feedthrough flange connects all internal electronics to the DAQ located outside

the pressure vessel. The four conduits house cables for the temperature sensors, the piezo electric transducers, and the heating plates. The fifth connection is used to drain mineral oil from the pressure vessel and compress the chamber.

The cold flange housing connects the lower two cooling coils (see Figure 43) to a chiller located outside the water tank. The cooling line is coupled to the large copper plate (see Figure 45) to keep the region inside the housing cold during operation. The housing itself is kept under vacuum, to prevent condensation and provide insulation. Included in the cold housing are the C_3F_8 fill/drain lines that are connected to two normally closed pneumatic valves. Connected to the left valve and open to the C_3F_8 volume is a PT, which sits just below the frame of the image. The PT measures the pressure in the C_3F_8; used with the PT in the instrumentation flanges to measure the pressure difference across the jars.

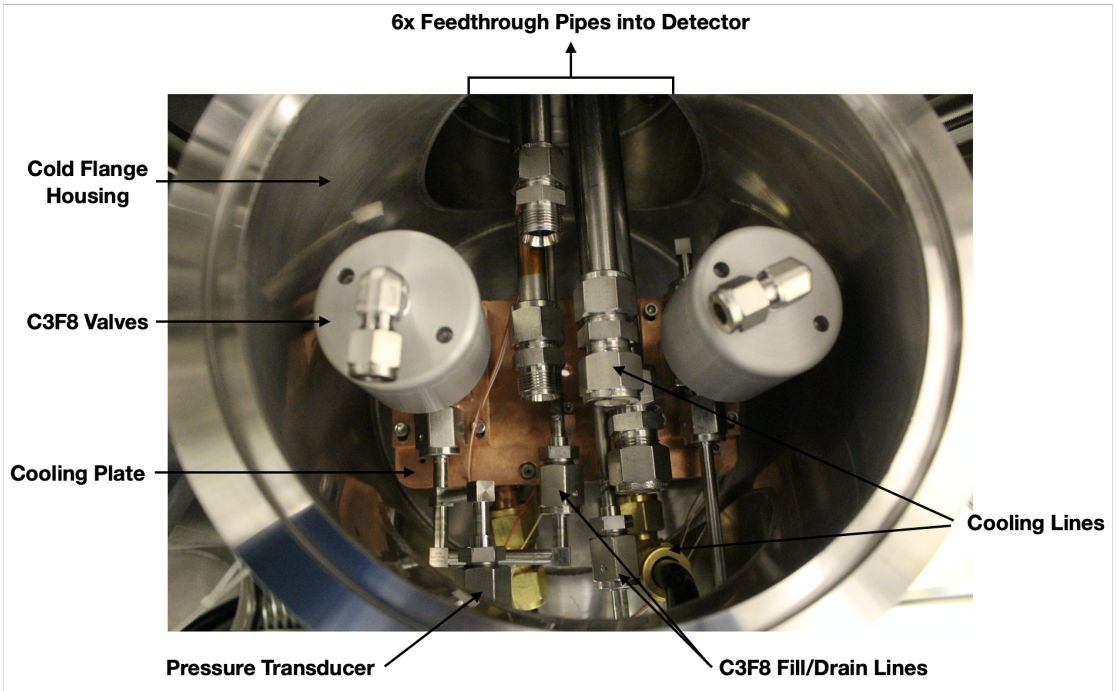

Figure 45: Cold flange housing. The four (unconnected) pipes leading out of the housing and the two brass connections to the copper plate, circulate chiller fluid to the cooling coils inside the detector. The two pneumatic valves are inline with the C_3F_8 to control the fill/drain of the detector. Connected to the left valve, open to the C_3F_8, is a PT used to measure the pressure inside the jars (sits below the field of view of the picture).

The base flange was installed in the water tank, followed by mounting the internals, making all the pipes/electrical connections, and assembling the insulation. Figure 46 shows this phase of installation. Visible in the image is the piezo mounting ring, which positions 12 sensors around the outer jar. Connected to the ring are two layers of HDPE sheets that fold into the top HDPE brick layer to avoid mineral oil passing between the two thermal regions. To prevent the glass jars from coming into contact with the large copper plate, HDPE bumpers are mounted to the bellows flange.

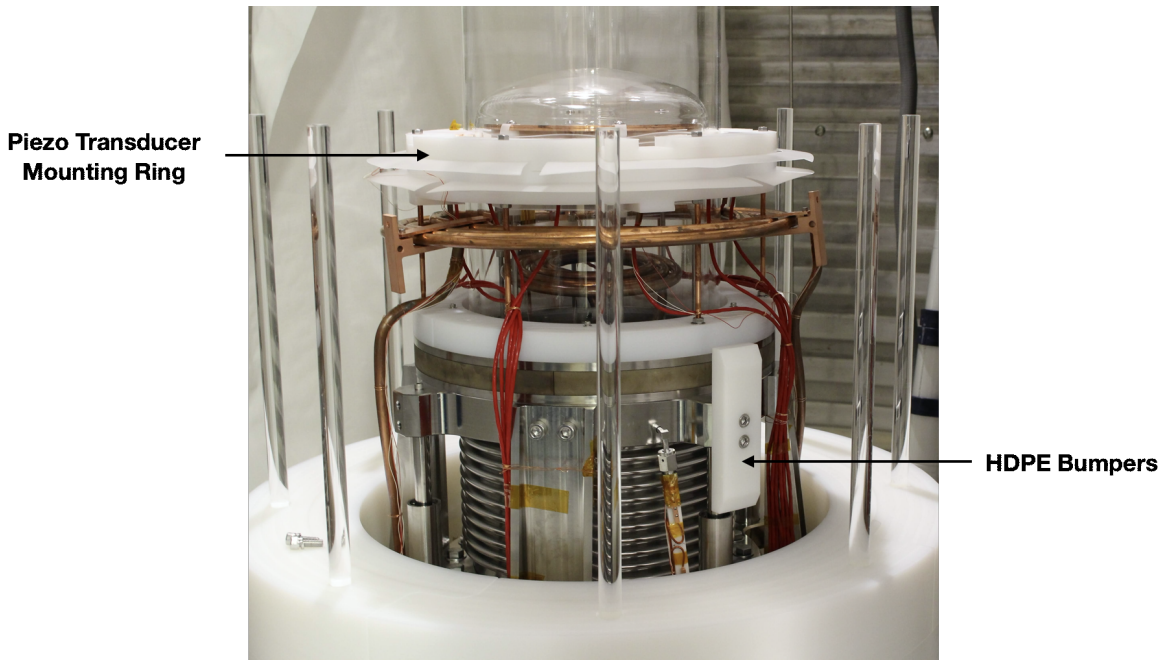

Figure 46: Installing the internals to the pressure vessel base inside the water tank. Here the HDPE piezo ring is mounted to the base flange, such that the 12 sensors are in contact with the outer jar. The ring includes HDPE sheets that prevent mineral oil convection. Added to the bellows are HDPE bumpers, which prevent horizontal motion of the detector to prevent the copper plate from coming into contact with the jars.

With all the HDPE components installed, the heater wire is fed into the top layer before mounting the copper plate (see Figure 47). The wires are held in place by Kapton tape, which also prevents direct contact with the copper plate.

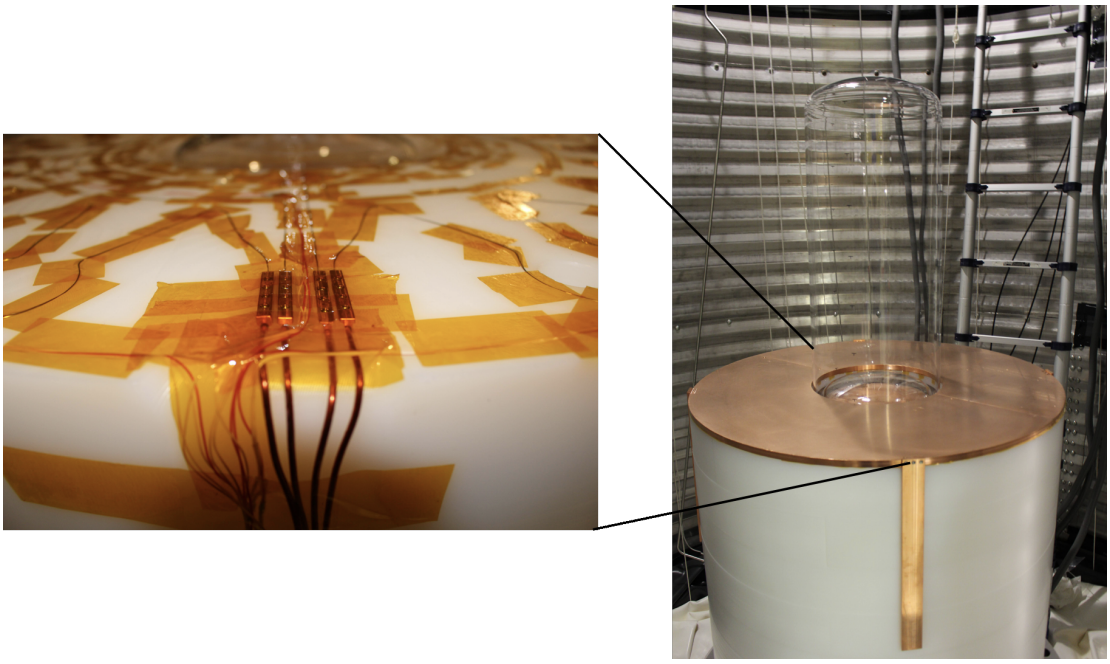

Figure 47: The heater wire is fed into groves cut out of the top layer of HDPE and held in place by Kapton tape, which also prevents direct contact between the wires and copper plate. The HDPE and copper components were machined at the University of Alberta in a radon reduced clean room [52], to minimize ^{252}Rn contamination.

The pressure vessel is then brought in and sealed to the base flange. The design of the pressure vessel includes an internal source tube (see Figure 42). This will allow calibration sources to be deployed close to the target fluid. The increased size of the vessel compared to PICO-60 keeps the radioactivity from the steel much farther away to minimize backgrounds.

The four camera enclosures each contain Basler acA1920-μm cameras, running at 150 fps. The cameras are mounted to a copper plate that connects to a cooling line (see Figure 48). The cooling line also connects to the copper LED ring, in direct contact with the view port. Also included in each enclosure is a compressed air line to prevent moisture buildup on the cameras and a humidity sensor to warn of water leaks.

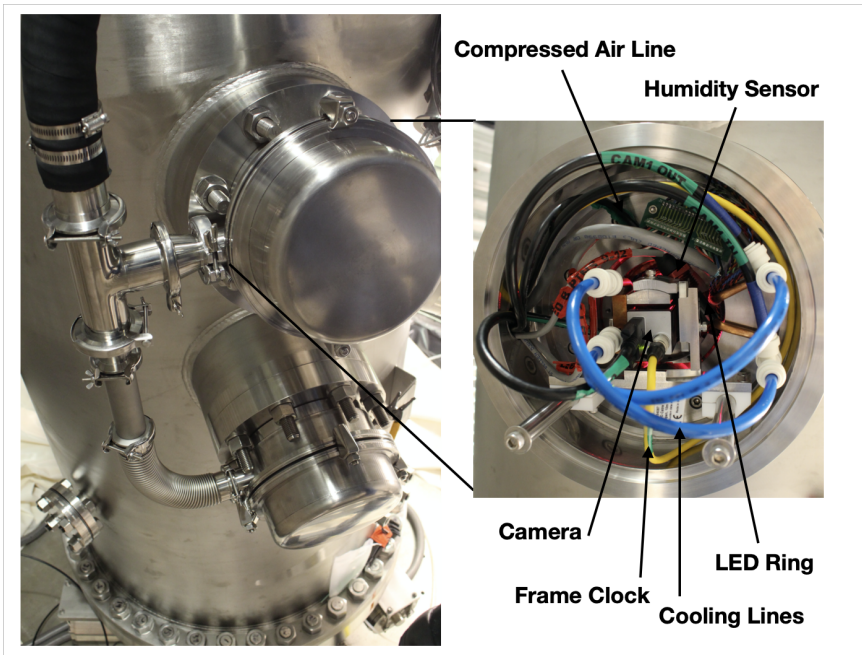

Figure 48: The camera enclosures are sealed off from the water tank environment. Each enclosure contains a camera mounted to a cooling plate. The cooling line also connects to the LED ring, which is in direct contact with the view port. The camera is connected to the main DAQ via a frame clock (yellow cable) and the camera server by USB3 (black cable). Also included is a compressed air line and humidity sensor.

The cameras are connected to dedicated servers via USB3. The cameras communicate with the main DAQ by a frame clock, which synchronizes image taking with the flashing LED rings. During a run, the images are actively checked for bubble formation. When a bubble in the detector is observed, the images surrounding the active frame are recorded and a trigger is initiated to the main DAQ and pressure programmable logic controller (PLC). The pressure PLC continuously monitors the pressure in the detector and activates the accumulators when triggered.

With the detector fully installed (figure 49) the mineral oil and C_3F_8 are filled, readying the detector for commissioning, data taking, and the water fill. Calibration sources can be deployed in either source tube. The internal one mentioned earlier is fed through the left tube, and there is an external source tube shown on the right.

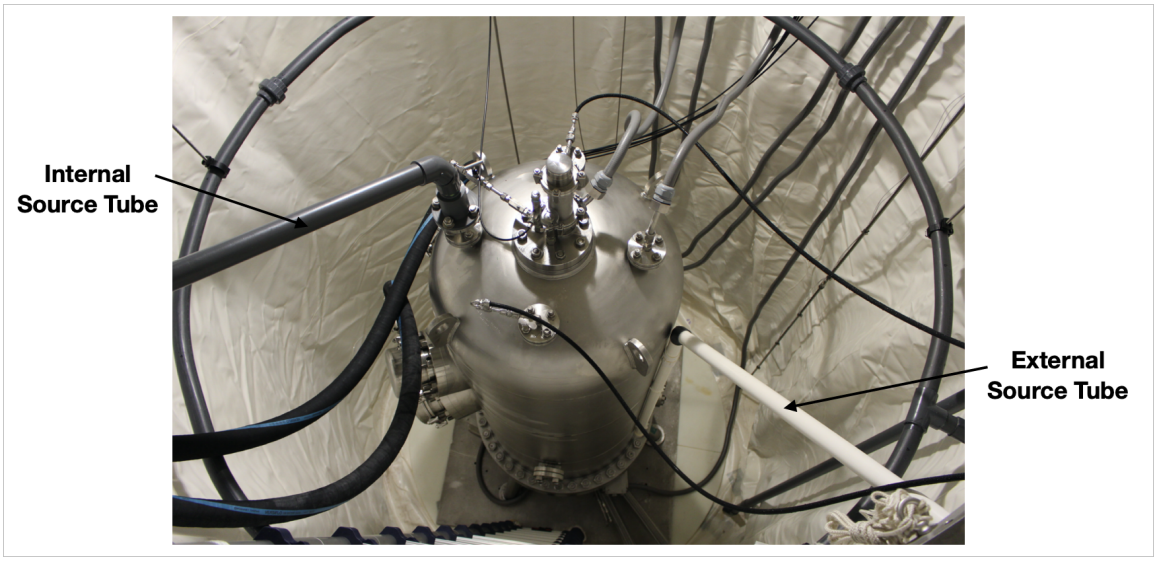

Figure 49: Detector is fully assembled with the water tank closed and the protective tank liner pulled up. The detector has two source tubes, the left one is fed into the pressure vessel and the right one sits outside the pressure vessel.

Without water, engineering data was collected to commission the detector. An example event is shown in Figure 50.

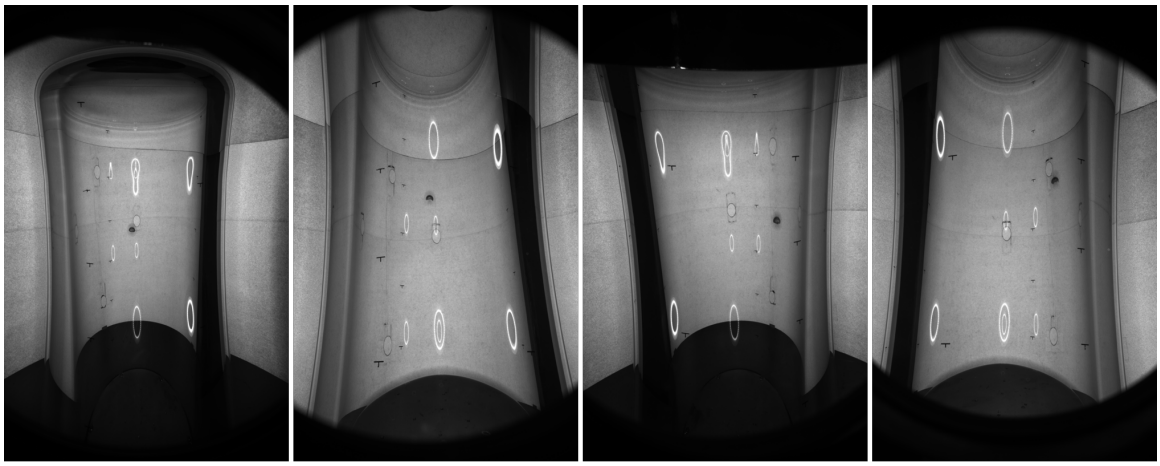

Figure 50: Engineering data collected during the DAQ commissioning. First glimpse of a single bubble event captured by PICO-40L (run 20200721_0 event number 0).

Figure 50 offers the first glimpse into the detector, which successfully captures bubble

formation and initiates the pressure cart to suppress continued boiling. Calibration data is planned once the water tank is filled and will include neutron sources to continue the neutron AP study presented in this thesis.

11 Conclusion

Neutrons are the primary background in moderately superheated C_3F_8 bubble chambers. These events are problematic, because they can be indistinguishable from a WIMP candidate. The research presented in this thesis concludes to which extent neutrons can be reconstructed in the PICO detectors, using energy, acoustic, and directional reconstruction techniques. The outcome demonstrated that primary neutron energy cannot be recovered using bubble multiplicity or the spread in a cluster from the center of gravity. This can be explained by neutron induced nuclear reactions, which produce an abundance of single bubble events for primary neutron energies exceeding 1.5 MeV. The total energy deposited from these nuclear reactions has an impact on the reconstructed acoustics, which PICO uses to identify background alphas from the decay of ^{222}Rn. By extending the molecular dynamics model for bubble expansion, the acoustic energy emitted from single bubble nuclear reactions was extrapolated. The analysis concluded that fast neutrons can fit on the log(AP) distribution outside the nuclear recoil and background alpha peaks. This provides a meaningful tool for future dark matter searches, because events in the tail of the AP distribution can be explained by neutrons, necessitating more neutron calibration data in future detectors. The remaining question for neutron reactions is direction reconstruction. The analysis technique attempted, minimized a line about the center of gravity for a bubble cluster. The goal was to determine if the direction of this line provided any information about the neutron source. This was answered by calculating the opening angle of this line with respect to the sources known position. Comparing the opening angle obtained from

Monte-Carlo and events reconstructed from the PICO-60 data, it was concluded that the line direction best resembled the random walk of a neutron. Therefore this technique cannot be used to predict the direction of a neutron source. The final work presented included key steps in the commissioning of the thermal and camera systems for PICO-40L. At the time of this thesis, engineering data has been collected and the water tank is being prepared for filling. This detector offers increased sensitivity to the dark matter search, and will be calibrated using neutron sources. These sources will provide an extended data set for the AP analysis of neutron reactions and multi-bubble events.

References

[1] Zwicky, F., Helvetica Physica Acta, Vol. 6, p. 110-127 (1933).

[2] Bartelmann, M. and Schneider, P., Phys. Rep. 340, 291-472 (2001).

[3] Planck Collaboration. AA https://doi.org/10.1051/0004-6361/201833880, (2019.)

[4] Slipher, V. M., Lowell Obs. Bull. 62, Vol. 11, 12 (1914).

[5] Wolf, M., Vierteljahresschr Astron. Ges. 49:162 (1914).

[6] Pease, F. G., Proc. Natl. Acad. Sci. USA, 4:21 (1918).

[7] Hubble, E. and Milton, L. H., Astrophysical Journal, Vol. 74, 43 (1931).

[8] Burbidge, E. M., et al., Astrophysical Journal, vol. 139, p.539 (1963).

[9] Begeman, K. G., Broeils, A. H. and Sanders, R. H., Monthly Notices of the Royal Astronomical Society, 249, 3 (1991).

[10] Soldner, J., Berliner Astron. Jahrb. p. 16l (1804).

[11] Eddington, A. S., "Space, Time and Gravitation", Cambridge University Press. Cambridge (1920).

[12] Zwicky, F., Phys. Rev., 51, 290 (1937).

[13] Zwicky, F., Phys. Rev., 51, 679 (1937).

[14] Walsh, D., et al., Nature 279, 381 (1979).

[15] Kneib, J., et al., Astrophys. Journal 471, 643 (1996).

[16] Hoekstra, H., et al., Astrophys. Journal 504, 636 (1998).

[17] Alpher, R. A., Bethe, H., and Gamow, G., Phys. Rev. 73, 803 (1948).

[18] Penzias, A. and Wilson, R., Astrophysical Journal, Vol. 142, p.419-421 (1964).

[19] Dicke, R., et al., Astrophysical Journal, Vol. 142, p.414-419 (1964).

[20] Olive, K. A., et al. (Particle Data Group), Chin. Phys. C 38, 090001 (2014).

[21] Jungman, G., Kamionkowski, M., and Griest, K., Phys. Rep. 267, 195 (1996).

[22] Goodman, M.W. and Witten, E., Phys. Rev. D 31,3059 (1985).

[23] Amole, C., et al., Phys. Rev. Lett. 118, 251301 (2017).

[24] Amole, C., et al., Phys. Rev. D 100, 022001 (2019).

[25] Felizardo, M., et al., Phys. Rev. D 89, 072013 (2014).

[26] Behnke, E., et al., Astropart. Phys. 90, 85 (2017).

[27] Akerib, D. S., et al., Phys. Rev. Lett. 116, 161302 (2016).

[28] Fu, C., et al., Phys. Rev. Lett. 118, 071301 (2017).

[29] Aprile, E., et al. Phys. Rev. D 99, 112009 (2019).

[30] Agnese, R., Anderson, A. J., Asai, M., et al. Phys. Rev. Let., 112(24) (2014).

[31] Ajaj, R., et al., Phys. Rev. D 100, 022004 (2019).

[32] Arnaud, Q., et al., Astroparticle Phys. 97, 54-62 (2018).

[33] Duncan, F., Noble, A. J., and Sinclair, D., Annu. Rev. Nucl. Part. Sci. 60, 163 (2010).

[34] Aharmim, B., et al, Rhys. Rev.D 80 012001 (2019).

[35] Gibbs, J.W., Ox Bow Press, Woodbridge, CT (1993).

[36] Seitz, F., Phys. Fluids 1, 2 (1958).

[37] Amole, C., et al., Phys. Rev. D 93, 052014 (2016).

[38] Lemmon, E. W., Huber, M. L., and McLinden, M. O., NIST. Standard Reference Database 23: Reference Fluid Thermo- dynamic and Transport Properties-REFPROP, Version 9.0, National Institute of Standards and Technology. Standard Reference Data Program, Gaithersburg (2010).

[39] Agostinelli, S., et al., Nucl. Instrum. Methods Phys. Res., Sect. A 506, 250 (2003); Allison J., et al., IEEE Trans. Nucl. Sci. 53, 270 (2006).

[40] National Nuclear Data Center (nndc.bnl.gov).

[41] Chadwick, M.B., et al., Nuclear Data Sheets. Volume 112, 12 (2011).

[42] Koning, A.J., et al., J. Korean Phys. Soc., 59, 2 (2011).

[43] Kluge, H. and Weise, K., Radiation Protection Dosimetry, 2, 2. Nuclear Technology Publishing (1982).

[44] Csikai, J. and Dezso, Z., Annals of Nuclear Energy, 3 (1976).

[45] Becchetti, F. D., et al., American Journal of Physics, 18, 112 (2013).

[46] Plimpton, S., Comput. Phys. 117, 1 (1995).

[47] Kozynets, T., Fallows, S., and Krauss, C., Phys. Rev. D 100, 052001 (2019).

[48] Jones, J.E., Proc. R. Soc. A 106, 463 (1924).

[49] Ziegler, J. F., Ziegler, M. D., and Biersack, J. P., Nucl. Instrum. Methods Phys. Res., Sect. B 268, 1818 (2010).

[50] Mitra, P., PICO-60: A Dark Matter Search Experiment with C_3F_8 in a Bubble Chamber. University of Alberta (2018.)

[51] PICO-40L Detector paper to be published.

[52] Hallin, A., et al, AIP Conference Proceedings 1338, 161 (2011).

[53] SNO Collaboration, Phys. Rev. C 72, 055502 (2005.)

Appendices

A Fiducial Volume and Data Quality Cuts

The complete PICO-60 data set includes events that cannot be used when analyzing either multiple or single bubble events. Further details available in [50].

The fiducial cut removes events originating from the walls of the quartz jar, associated with impurities on the jar surface. This cut also removes events on the interface between the water and C_3F_8.

The second set of cuts check for data quality. This ensures the pressure and temperature measured at the time of the event is consistent, while also checking that there are no timeouts, missing information, or poor acoustic measurements associated with the event.

The final cuts are dependent on the events being studied, selecting either multiples or single bubble events and the data run. The bubble multiplicity is identified by the number of bubbles found in the image and is referenced to the Dytran signal. The run type is selected using a number PICO assigned. For example, the 60 cm ^{252}Cf run is 15, so cutting all but run 15 returns the events specific to that data set.

B Estimating the Calibration Source Strength

The AmBe and ^{252}Cf calibration sources used for PICO-60 are designated SLB024 and SLB018 within internal SNOLAB documentation.

B.1 AmBe: SLB024 neutron source

The AmBe source strength was documented on December 6th 2007, with a neutron yield of 68.70 $\pm$ 0.74 neutrons per second. With a half-life of 432.2 years, the radioac-

tivity at the time of deployment, September 23rd 2016, will be slightly less then the 2007 measurement. The new rate, A, is calculated by:

$$A(t) = A_0 e^{-t/\tau}, \tag{16}$$

with an uncertainty given by:

$$\delta A = \delta A_0 e^{-t/\tau}. \tag{17}$$

Where A_0 is the 2007 rate, t is the number of years since that measurement, and τ is the half life of the AmBe source. The calibration run took place 3215 days since 2007, therefore the AmBe rate is 67.3 $\pm$ 0.7 neutrons per second.

B.2 ^{252}Cf: SLB018 neutron source

The ^{252}Cf source strength was measured by the SNO collaboration on July 12, 2001 as 16.55 $\pm$ 0.08 neutrons per second [53]. With a half-life of 2.654 years, the activity for PICO-60, deployed between November 8th 2016 to January 19th 2017, cannot be assumed consistent with this measured rate.

To estimate the source strength 15 years later, the fallowing calculation is used:

$$A(t) = A_0 \left(e^{-t/\tau_{252}} + f_{250}(e^{-t/\tau_{250}} - e^{-t/\tau_{252}}) \right). \tag{18}$$

A_0 is the activity on July 12, 2001. f_{250} is the fraction of ^{250}Cf present in the ^{252}Cf source; documented by SNO as 0.0192 $\pm$ 0.0002. The half-life for ^{250}Cf and ^{252}Cf are: τ_{250} = 13.08 years and τ_{252} = 2.654 years respectfully. t is the number of years since the source was measured in 2001.

The uncertainty is calculated using:

$$\delta A(t) = \delta A_0 e^{-t/\tau_{252}} + A_0 f_{250} \sqrt{\left(\frac{\delta A_0}{A_0}\right)^2 + \left(\frac{\delta f_{250}}{f_{250}}\right)^2} \left(e^{-t/\tau_{250}} - e^{-t/\tau_{252}}\right). \qquad (19)$$

Between July 12th 2001 and November 8th 2016 there are 5629 days or 15.4 years. The estimated source activity is therefore: 0.145 ± 0.001 neutrons per second, or 8.72 ± 0.08 neutrons per minute.